

AT2019wxt: An ultra-stripped supernova candidate discovered in electromagnetic follow-up of a gravitational wave trigger

HINNA SHIVKUMAR,¹ AMRUTA D. JAODAND,² ARVIND BALASUBRAMANIAN,³ CHRISTOFFER FREMLING,² ALESSANDRA CORSI,³ ANASTASIOS TZANIDAKIS,⁴ SAMAYA NISSANKE,^{5,6} MANSI KASLIWAL,² MURRAY BRIGHTMAN,⁷ GEERT RAALJMAKERS,⁵ KRISTIN KRUSE MADSEN,⁸ FIONA HARRISON,² DARIO CARBONE,⁹ NAYANA A.J.,¹⁰ JEAN-MICHEL DÉSSERT,¹ AND IGOR ANDREONI^{11,12,13}

¹*Anton Pannekoek Institute for Astronomy, University of Amsterdam, Science Park 904, 1098 XH, Amsterdam, The Netherlands*

²*California Institute of Technology, 1200 E California Blvd., Pasadena, CA 91125, USA*

³*Department of Physics and Astronomy, Texas Tech University, Box 1051, Lubbock, TX 79409-1051, USA*

⁴*University of Washington, 3910 15th Avenue NE, Seattle, WA 98195, USA*

⁵*GRAPPA, Anton Pannekoek Institute for Astronomy and Institute of High-Energy Physics, University of Amsterdam, Science Park 904, 1098 XH Amsterdam, The Netherlands*

⁶*Nikhef, Science Park 105, 1098 XG Amsterdam, The Netherlands*

⁷*California Institute of Technology, 1200 E California Blvd., Pasadena, CA 91125, USA*

⁸*CRESST and X-ray Astrophysics Laboratory, NASA Goddard Space Flight Center, Greenbelt, MD 20771 USA*

⁹*University of the Virgin Islands, 2 Brewers Bay Road, Charlotte Amalie, USVI 00802, USA*

¹⁰*Indian Institute of Astrophysics, II Block, Koramangala, Bangalore 560034, India.*

¹¹*Joint Space-Science Institute, University of Maryland, College Park, MD 20742, USA*

¹²*Department of Astronomy, University of Maryland, College Park, MD 20742, USA*

¹³*Astrophysics Science Division, NASA Goddard Space Flight Center, Mail Code 661, Greenbelt, MD 20771, USA*

ABSTRACT

We present optical, radio and X-ray observations of a rapidly-evolving transient AT2019wxt (PS19hgw), discovered during the search for an electromagnetic (EM) counterpart to the gravitational-wave (GW) trigger S191213g (LIGO Scientific Collaboration & Virgo Collaboration 2019a). Although S191213g was not confirmed as a significant GW event in the off-line analysis of LIGO-Virgo data, AT2019wxt remained an interesting transient due its peculiar nature. The optical/NIR light curve of AT2019wxt displayed a double-peaked structure evolving rapidly in a manner analogous to currently known ultra-stripped supernovae (USSNe) candidates. This double-peaked structure suggests presence of an extended envelope around the progenitor, best modelled with two-components: i) early-time shock-cooling emission and ii) late-time radioactive ⁵⁶Ni decay. We constrain the ejecta mass of AT2019wxt at $M_{ej} \approx 0.20M_{\odot}$ which indicates a significantly stripped progenitor that was possibly in a binary system. We also followed-up AT2019wxt with long-term *Chandra* and Jansky Very Large Array observations spanning ~ 260 days. We detected no definitive counterparts at the location of AT2019wxt in these long-term X-ray and radio observational campaigns. We establish the X-ray upper limit at 9.93×10^{-17} erg cm⁻² s⁻¹ and detect an excess radio emission from the region of AT2019wxt. However, there is little evidence for SN1993J- or GW170817-like variability of the radio flux over the course of our observations. A substantial host galaxy contribution to the measured radio flux is likely. The discovery and early-time peak capture of AT2019wxt in optical/NIR observation during EMGW follow-up observations highlights the need of dedicated early, multi-band photometric observations to identify USSNe.

1. INTRODUCTION

Massive stars at the endpoints of their lives undergo mass loss through ejection of some or all of their hydrogen (and possibly helium) envelopes, eventually collapsing in what are known as stripped-envelope core-collapse supernovae (SESNe, Filippenko 1997; Gal-Yam et al. 2014). The extent to which the outer layers of massive stars are stripped dictates their

spectroscopic classification into their various sub-classes. Partial stripping in Type IIb SNe is supported by the presence of Balmer lines while strong stripping in Type Ic SNe is evident by absence of both Hydrogen and Helium lines. The current population of SESNe suggests that ejection of the progenitor envelopes can be driven by a) mass loss via stellar-wind (Begelman & Sarazin 1986; Woosley & Weaver 1995; Pod 2001), or b) mass transfer during binary interaction (Podsiadlowski et al. 1992; Yoon et al. 2010; Smith et al. 2011; Yoon 2017).

Large uncertainties currently persist in our understanding of the progenitors of SESNe. Specifically, if any links exist between the various SESNe sub-classes, and if different sub-

classes have preferred mass loss mechanisms. At the same time, the observational picture of SESNe has been evolving in the last few years as wide-field optical surveys have accelerated the rate of discovery and started filling-up the luminosity “gap” between novae and SNe in the luminosity-duration phase-space (Nugent et al. 2015). In particular, optimized follow-up observations have opened up the parameter space for characterisation of rapidly-evolving, low-luminosity ($L_{bol} = 10^{42}$ erg/s) transients – resulting in a growing population of ultra-stripped SNe (USSNe Kasliwal et al. 2010; Drout et al. 2013; De et al. 2018a; Jacobson-Galán et al. 2020; De et al. 2018b).

The progenitors of USSNe undergo extreme envelope stripping via two stages of common envelope evolution, with a first phase of mass-transfer through Roche-Lobe overflow, leading to a He-star NS system. The second mass-transfer phase in the resulting He-star NS system involves stripping of the He-star leading to a stripped He-star NS system with a He-rich envelope. The core-collapse of the stripped He star triggers a maximally stripped SN explosion known as USSN. This explosion is accompanied by ejection of $\approx 0.01M_{\odot}$ of the star mass. Such USSN are then expected to evolve into binary neutron star (BNS) systems (Tauris et al. 2013, 2015, 2017). In fact, light curves of these SNe display double peaks in both bluer and redder bands, indicating presence of an extended envelope around the progenitor (Nakar & Piro 2014). The combination of shock-cooling emission (SCE) and radioactive decay of ^{56}Ni has been used to explain this double-peaked structure and rapid evolution in the light curves of currently known USSNe candidates such as SN2019dge (Yao et al. 2020) and iPTF14gqr (De et al. 2018b).

In this work, we present multi-wavelength observations spanning optical, radio and X-ray wavebands for one such puzzling USSN candidate dubbed AT2019wxt. AT2019wxt was discovered by the PanSTARRS Search for Kilonovae survey (as PS19hgw) during their EM follow-up of LIGO-Virgo GW trigger, S191213g (flagged as a BNS merger event; LIGO Scientific Collaboration & Virgo Collaboration 2019a). A follow-up observational campaign across the EM spectrum was encouraged because AT2019wxt was located in the 80% confidence contour of the S191213g’s skymap (LIGO Scientific Collaboration & Virgo Collaboration 2019b) with its distance being consistent with estimated luminosity distance range for S191213g (McBrien et al. 2019a). Moreover, the optical light curve of AT2019wxt displayed a very fast decline in comparison to previously known rapidly-evolving, hydrogen-free supernovae such as SN2008ha or SN2010ae (Valenti et al. 2009; Foley et al. 2009; Stritzinger et al. 2014). Although, in offline analysis of GW data S191213g was demoted as a significant GW candidate (The LIGO Scientific Collaboration et al. 2021), AT2019wxt remains a very interesting transient. Our multi-band optical observations show a double-peaked rapidly-declining light curve resembling that of the USSNe candidates iPTF14gqr (De et al. 2018b) and SN2019dge (Yao et al. 2020).

We outline the interesting nature of AT2019wxt based on a campaign of high-cadence optical observations and other complementary data from radio and X-ray observational campaigns. Our work is organized as follows. Section 2 outlines the observational properties of AT2019wxt and its multi-band follow-up observations. Section 3 outlines the data analysis techniques used for optical, X-ray and radio observations. Here, we also present a fully Markov-Chain Monte-Carlo (MCMC) parameter estimation for characterization of AT2019wxt’s physical properties. Finally, in section 4, we provide interpretation of results obtained from this comprehensive dataset and their implications in the broader context of stellar evolution.

2. DISCOVERY AND PANCHROMATIC FOLLOW UP

2.1. AT2019wxt (PS19hgw)

AT2019wxt was discovered on 2019 December 16 UTC 07:19:12 (MJD 58833.305) as a source at an optical magnitude of 19.38 ± 0.05 in the PS1 *i*-band (McLaughlin et al. 2019; McBrien et al. 2019a). It was localised to RA = 01:55:41.941, Dec = +31:25:04.55 and found to be associated with the compact host galaxy, KUG 0152+311¹. The association of AT2019wxt with KUG 0152+311 was confirmed by early optical spectra (Dutta et al. 2019), which displayed standard galaxy lines at a redshift of $z=0.036$ (luminosity distance, $d = 144$ Mpc). This distance estimate from optical observations placed AT2019wxt within 80% confidence interval of LIGO-VIRGO localisation skymap (at a luminosity distance range of S191213g $d_L=201\pm 81$ Mpc; McBrien et al. 2019a; LIGO Scientific Collaboration & Virgo Collaboration 2019b). The offset between AT2019wxt and the host galaxy was observed to be $0.5''\text{S}, 7.7''\text{E}$ with a projected a distance of 6.7 kpc from the galactic center (McLaughlin et al. 2019).

The presence of Helium in optical spectra and rapid photometric evolution further confirmed AT2019wxt as an interesting EM candidate counterpart of S191213g. The rapid decline in brightness was observed to be faster than that for known hydrogen-free SNe (e.g. SN2008ha, SN2010ae Valenti et al. 2009; Foley et al. 2009; Stritzinger et al. 2014) but slower than the kilonova AT2017gfo associated with GW170817 (e.g. Arcavi et al. 2017a; Cowperthwaite et al. 2017) and the possible white dwarf-neutron star (WD-NS) merger SN2018kzr (McBrien et al. 2019b; Huber et al. 2019). Hence, we triggered a comprehensive, multi-band EM follow-up campaign with a host of space and ground-based telescopes. This observational campaign spanned optical/near-Infrared (NIR), X-ray, and radio wavebands. Observations for each of these wavebands are summarized in Tables 7, 8, 9, and 10, respectively.

2.2. Optical/NIR Observations

¹ Galaxy morphology and classification from NASA/IPAC Extragalactic Database (NED) <http://ned.ipac.caltech.edu>. Please also refer to Gaia Collaboration (2020)

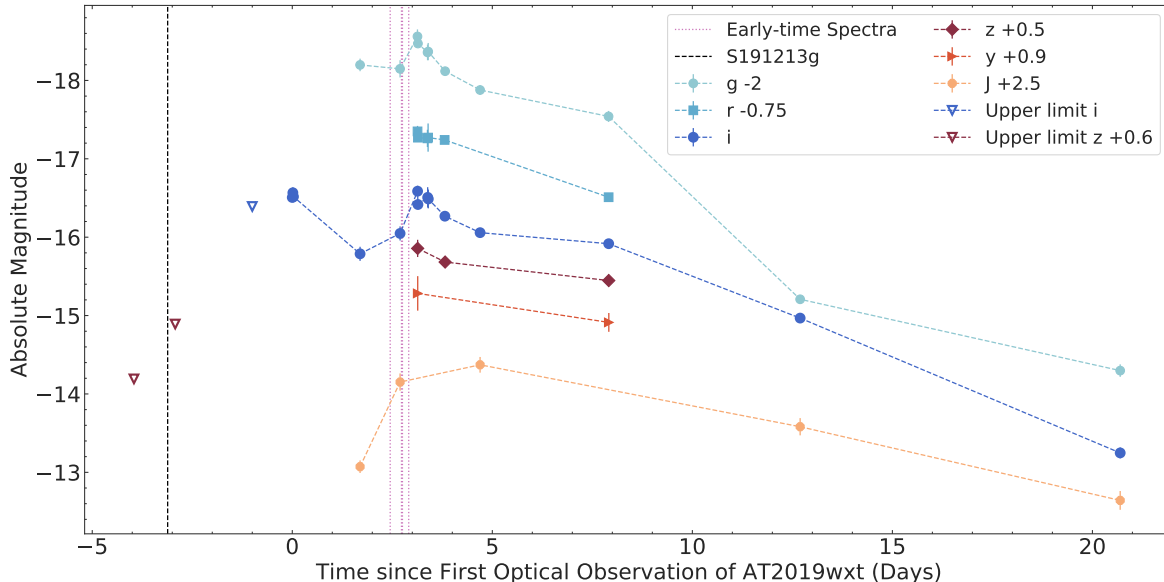


Figure 1. Galactic extinction corrected optical and NIR light curves of the transient AT2019wxt, using the data from Table 7. The cyan, light blue, blue, magenta, dark red, orange, and yellow markers represent photometric data in the g , r , i , z , y , and J bands, respectively and the markers for each band are connected by a dashed line to visually track the photometric evolution. The magnitudes are offset vertically for better visibility and the times displayed are relative to the first optical observation at MJD 58833.305, used as a reference epoch henceforth. The vertical black dashed line indicates the time of the GW trigger S191213g, for reference. Vertical, dotted, magenta lines indicate epochs where early-time spectroscopic observations used in this work (see, 2.2.2).

2.2.1. Photometric Observations

After the initial discovery of AT2019wxt was reported by PanSTARRS (McLaughlin et al. 2019; McBrien et al. 2019a), the Global Relay of Observatories Watching Transients Happen (GROWTH) collaboration conducted further follow-up observations using the Spectral Energy Distribution Machine (SEDM; Blagorodnova et al. 2018) on the Palomar 60-inch (P60 Cenko et al. 2006) telescope. The SEDM obtained 180 s exposure time images of AT2019wxt with the rainbow camera imager for each of the $ugri$ filters. These images were processed using a standard python-based and fully automated reduction pipeline FPipe (Fremling et al. 2016), which performs host-galaxy subtraction and PSF fitting photometry. Host-galaxy subtraction was performed using SDSS images of KUG 0152+311, and the source photometry was derived in the AB magnitude system (Fremling 2019).

The GROWTH collaboration also obtained 300 s exposure images in g , r and i filters with the Lulin 1-m Telescope (LOT) located in Taiwan. The LOT magnitudes, also in the AB magnitude system, are calibrated against the PS1 catalog (Kong 2019). Follow-up observations of AT2019wxt were also conducted with the Large Monolithic Imager (LMI) (Bida et al. 2014) on the 4.3m Lowell’s Discovery Channel Telescope (DCT, located in Arizona) for each of the $griz$ filters. The magnitudes are calibrated with the SDSS catalog and are presented in the AB system (Dichiara & a larger Collaboration 2019). Simultaneously, optical observations of AT2019wxt were also undertaken with the three channel imager 3KK camera (Lang-Bardl et al. 2016) on 2m telescope at the Wendelstein

Observatory. Observations were obtained on 5 epochs for each of the filters (g' , i' , J). Aperture photometry was performed using eight comparison stars within the field of view of the detector. Magnitude errors include statistical error in the measurement of the magnitude of AT2019wxt and in the zero-point calculation (Hopp et al. 2020).

The observations and photometric measurements are summarized in Table 7 and span ≈ 20.7 days since initial detection. The multi-band light curves are collectively displayed in Figure 1. We corrected apparent magnitudes for Galactic extinction, using the data available on the foreground galactic extinction for the host galaxy KUG 0152+311 on the NASA/IPAC Extragalactic Database (NED) for each band. The NED calculates Galactic extinction values assuming the Fitzpatrick (1999) reddening law with $R_V \equiv A(V)/E(B - V) = 3.1$.

2.2.2. Spectroscopic Observations

Early-time spectroscopic observations of AT2019wxt were taken on 2019 December 18 and 19 (see, Table 8). The initial spectroscopic observations were unable to firmly classify the transient (Dutta et al. 2019; Izzo et al. 2019; Srivastav & Smartt 2019). AT2019wxt showed narrow lines consistent with the host galaxy redshift of $z=0.037$, and a blue, relatively featureless continuum with a broad feature at 5400 - 6200 Å. Vogl et al. (2019) identified the broad feature as HeI lines, and suggested that AT2019wxt was either a young Type Ib or perhaps Type IIb supernova given the blue continuum. The similarities of the spectra to SN 2011fu (Kumar et al. 2013) prompted Valley (2019) to classify AT2019wxt as a type IIb. This super-

nova classification was subsequently supported by Valeev et al. (2019) and Becerra-Gonzalez & a larger Collaboration (2019).

In this work we use early-time spectroscopic observations obtained with various telescopes such as: i) 2 m Himalayan Chandra Telescope (HCT) at Indian Astronomical Observatory at Hanle, ii) 8.2 m Very Large Telescope (VLT) UT1 at European Southern Observatory (ESO) at La Silla, Chile, iii) 3.58 m New Technology Telescope (NTT) as part of the ePESSTO extended-Public ESO Spectroscopic Survey for Transient Objects (PI:Smarrt), and iv) 8.4 m The Large Binocular Telescope (LBT) at LBT Observatory in Arizona, USA. The HCT observations were conducted with Hanle Faint Object Spectrograph Camera (HFOSC2) instrument (Dutta et al. 2019). HCT/HFOSC2 provides low to medium resolution grism spectroscopy with resolution of 150 to 4500 based on grism settings. HCT observations in this work used grism 7 was to provide a resolution of 1200 for the observations in the wavelength range of 3800-7500 Å. The VLT observations were carried out with FOCal Reducer/low dispersion Spectrograph 2 (FOS2) instrument on UT1 Cassegrain focus in long-slit mode (slit-width of 418.57") to obtain spectroscopic observations of AT2019wxt (Vogl et al. 2019). The long-slit mode provides resolution of 260-2600. ESO-NTT was used with ESO Faint Object Spectrograph (EFOS) on Nasmyth B focus (Müller Bravo et al. 2019). EFOS provides low-resolution spectroscopy of faint objects. The LBT was used with Multi-Object Double Spectrograph which provides a spectral resolution 103 to 104 (Vallely 2019).

2.3. X-ray Observations

We obtained high resolution (~ 1 arcsec) X-ray imaging observations of AT2019wxt with *Chandra* X-ray. These observations were performed with back-illuminated Advanced CCD Imaging Spectrometer (ACIS) ² chip S3 in timing exposure (TE) mode. The ACIS S3 chip provided energy resolution of 95 eV (at 1.49 keV) at aim-point (in this case, S3 chip), timing resolution of 3.2 s, and a field-of-view (FOV) of 8.3×8.3 arcmins. The TE mode allowed for Very Faint (VF) telemetry format which reduced background contamination especially at lower and higher energy ranges for low count rate and/or extended sources.

Our trigger criterion for these *Chandra* observations was a well-localised (\sim few arc-seconds) BNS merger within 200 Mpc. At the time of initial discovery, AT2019wxt was a primary and interesting candidate counterpart to S191213g given the reddening and photometric evolution. Moreover, the host galaxy redshift firmly placed it within 3σ (100 Mpc) of the S191213g candidate (201 ± 81 Mpc; LIGO Scientific Collaboration & Virgo Collaboration 2019b). Extrapolating from GW170817 (Haggard et al. 2017), we expected at least 10 photons in one 100 ks exposure. The observations were scheduled to span 6 months period post initial GW trigger (a

detailed summary of the observations can be found in Table. 9). This timescale was motivated by continued X-ray observations of GW170817, 3.5 yrs post the BNS merger event (Hajela et al. 2022). Given lower total mass prediction for S191213g than GW170817, we expected a long-lived supermassive or stable NS remnant with X-ray emission from the magnetar wind nebula emerging at later times, and hence continued the AT2019wxt follow-up.

2.4. Radio Observations

Radio observations of the AT2019wxt field were carried out using the Karl G Jansky Very Large Array (VLA) between UT 19 December 2019 and 20 August 2020 in the D (VLA:19A-222, PI:Troja), C and B configurations (VLA:18B-320 and VLA:20A-115, PI: Frail). These observations were performed at nominal central frequencies of 10 GHz (X-band), 15 GHz (Ku-band), 22 GHz (K-band), and are summarised in Table 10. The raw data were calibrated using the CASA (McMullin et al. 2007) automated calibration pipeline and imaging analysis was performed using the CASA task `tclean`. The relative observational epochs in column two of Table 10 are with respect to the first optical detection (reference epoch; MJD 58833.305).

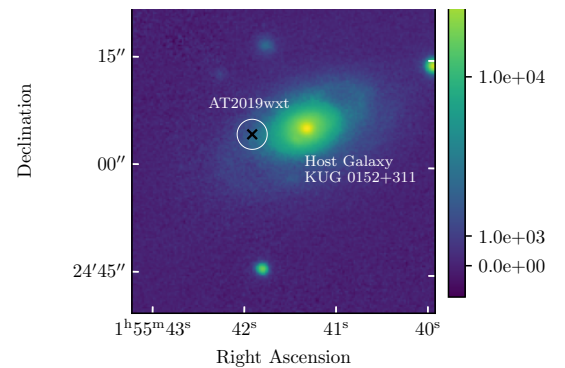


Figure 2. Pan-STARRS i-band image overplotted with the position of AT2019wxt (cross marks the optical position) and a circle of radius 2.1'' along with extent of the host galaxy KUG 0152+311.

In Table 10 we also present flux densities of AT2019wxt and its host galaxy KUG 0152+311 (in units of $\mu\text{Jy} = 10^{-29} \text{ erg s}^{-1} \text{ cm}^{-2} \text{ Hz}^{-1}$). The flux density of AT2019wxt is the maximum value obtained from a circular region of one nominal synthesised beam width³ centered on AT2019wxt using the CASA task `imstat`. Using this same task in the residual image, we computed root mean square (RMS) flux density within a 30'' circular region centered on AT2019wxt. The flux calibrator, 3C48, used in these computations has been undergoing a flare since January 2018⁴. Hence, we added additional 10% (X and Ku bands) and 20% (K-band) absolute flux calibration

² for more details please refer to Chapter 6 of Proposers' Observatory Guide, Cycle 24

³ <https://science.nrao.edu/facilities/vla/docs/manuals/oss/performance/resolution>

⁴ <https://science.nrao.edu/facilities/vla/docs/manuals/oss/performance/fdscalc>

errors in quadrature to the above RMS values. These final flux density errors are presented in the Table 10. Any observation with resulting flux density lower than $3\times$ the final flux density error were designated as upper limits. All K-band observations are therefore upper limits.

We then obtained the peak flux density of the host galaxy KUG 0152+311 from CASA task `imstat` in circular regions of radii $2.1''$ (X-band), $1.4''$ (Ku-band) and $3.1''$ (K-band), centred at $01h55m41.363s$, $31h25m05.06s$ in all configurations (so as to account for extended emission from the host, see Fig. 2). Absolute flux calibration errors as described above were added in quadrature to the RMS value obtained from the large 30 arcsec region around AT2019wxt to obtain the error on the galaxy’s peak flux density.

3. DATA ANALYSIS & RESULTS

3.1. Optical/NIR Data Analysis

3.1.1. Light curve Evolution

The earliest optical detection of AT2019wxt was obtained in i -band and the light curve in this band displayed a prominent double-peaked structure (evident from Figure 1). While g -band confirms a similar double-peaked structure, we only observe the tail-end of first peak due to lack of early-time observations. We lack early-time observations during the rise to the second peak in the r , z and y bands, so in these bands we can only report a decline in brightness relative to the time of the second peak in g and i bands.

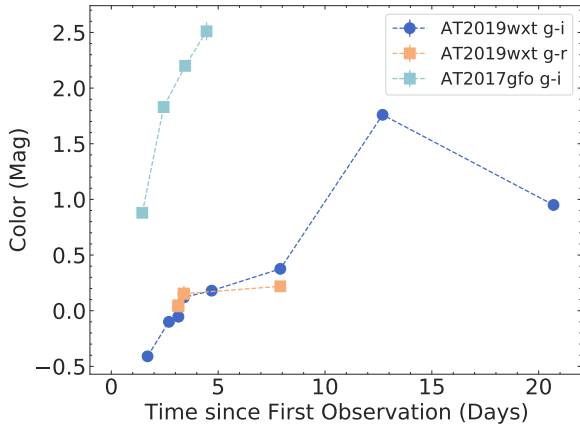


Figure 3. Color evolution of AT2019wxt compared to that of the GW170817 post-merger kilnova, AT2017gfo. Blue solid circles show the $g-i$ color evolution for AT2019wxt and orange filled squares show the $g-r$ color evolution for AT2019wxt. A reddening through the $g-i$ color evolution is observed followed by a peak at ~ 13 days post initial transient detection. Meanwhile, cyan filled squares and dashed connector lines between them show the $g-i$ color evolution for AT2017gfo.

The rate of evolution of the optical light curve is quite rapid and comparable to the previously known fastest, extra-galactic transients (further discussed in Sec. 4). For example, in the i -band, the first peak ($M_{i, \text{peak1}} \approx -16.5 \pm 0.05$ mag) displays a rapid decline in brightness, reaching a minimum within ≈ 1.7

days. A subsequent rebrightening is then observed which leads to a second peak ($M_{i, \text{peak2}} \approx -16.6 \pm 0.07$ mag) at ≈ 3.1 days since initial detection. After the second peak, the light curves exhibit a rapid decline in the bluest bands (g, i), whereas a relatively shallow (≈ 0.108 mag day^{-1}) decline is seen in the redder NIR J -band. Although, we note that this shallow decline may just be a result of a lack of observations in the J -band. Interestingly, a non-uniform behavior in the light curve evolution is observed post the second peak. It can be characterised by an initial rapid decline up to ≈ 5 days at average rate of ≈ 0.43 mag day^{-1} in the g -band and ≈ 0.27 mag day^{-1} in the i -band. Following this phase, we observe a decline in the light curve that is relatively slower and accompanied by a shoulder at ≈ 8 days. This long-term evolution of the light curve is visible in the g , i and J bands. It should be noted that a similar behaviour with distinct evolution rates between redder and bluer bands has been observed for the kilonova AT2017gfo (Cowperthwaite et al. 2017).

To understand the color evolution of AT2019wxt we calculated $g-i$ and $g-r$ colors. To achieve this we initially grouped together observations from different bands performed either simultaneously or on the same day. The colour evolution obtained as such is displayed in Figure 3 and shows $g-i$ color reddening from 1.7 days to about 6 days at a rate of ≈ 0.13 mag day^{-1} . This color evolution is slower than that of the kilonova AT2017gfo. This further confirms the distinct and complex evolutionary behavior across different bands.

3.1.2. Spectral Energy Distribution

We construct the spectral energy distribution (SED) of AT2019wxt using multi-band photometric observations spanning $grizyJ$ bands. We first grouped these observations from

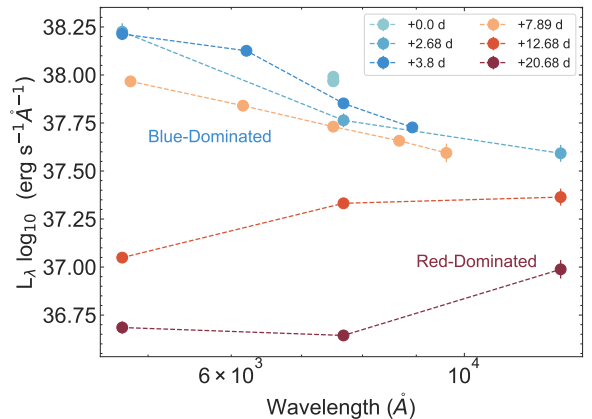


Figure 4. The spectral energy distribution of AT2019wxt at six representative epochs. The cyan, light blue, blue, yellow, dark red and magenta circular markers represent six different epochs, respectively in an increasing order and the markers for each epoch are connected by a dashed line to visually track the evolution of the SED. The early-time emission peaks at bluer wavelengths and we observe a rapid transition to redder wavelengths at late-time. All times are relative to first optical observation as a reference epoch.

different bands which were performed either simultaneously or on the same day. Of the resulting nine epochs, we present six epochs in Fig. 4 to compare the temporal evolution of the SED of AT2019wxt.

Initially, emission at bluer wavelengths dominates the SED, and over time, we observe a peak shift to redder wavelengths. Assuming the transient emits as a blackbody, as a first-order approximation we fit a blackbody model to the SED at each epoch using the MCMC implementation via `emcee` package⁵ (Foreman-Mackey et al. 2013). This package uses an MCMC ensemble sampler immune to affine transformations (Goodman & Weare 2010). Resulting SED and blackbody fits for each epoch are shown in Figure 5. Our MCMC implementation also yielded the blackbody radius (R_{bb}) and temperature of the blackbody T_{bb} at each epoch. The bolometric luminosity, L_{bol} , is then calculated using these parameters (see, Table 1) with a simple Stefan-Boltzmann law. We also show evolution of L_{bol} , T_{bb} and R_{bb} in Figure 6.

Epoch (MJD)	$\log_{10}L_{\text{bol}}$ (erg s ⁻¹)	R_{bb} (10^3R_{\odot})	T_{bb} (10^3K)
58833.3	42.29 ^{+2.79} _{-1.47}	9.06 ^{+12.32} _{-19.12}	9.12 ^{+27.95} _{-7.38}
58835.0	42.01 ^{+0.09} _{-0.09}	5.72 ^{+0.54} _{-0.57}	9.77 ^{+0.79} _{-0.73}
58836.0	42.05 ^{+0.13} _{-0.13}	11.41 ^{+1.81} _{-1.79}	7.08 ^{+0.71} _{-0.69}
58836.4	42.13 ^{+0.05} _{-0.05}	9.06 ^{+0.54} _{-0.54}	8.32 ^{+0.32} _{-0.31}
58837.1	42.01 ^{+0.02} _{-0.02}	9.06 ^{+0.19} _{-0.19}	7.76 ^{+0.11} _{-0.11}
58838.0	41.97 ^{+0.07} _{-0.07}	11.41 ^{+1.02} _{-1.04}	6.76 ^{+0.34} _{-0.33}
58841.2	41.77 ^{+0.05} _{-0.05}	11.41 ^{+0.79} _{-0.79}	6.03 ^{+0.23} _{-0.23}
58846.0	41.53 ^{+0.05} _{-0.05}	22.76 ^{+1.59} _{-1.67}	3.72 ^{+0.08} _{-0.08}
58854.0	40.77 ^{+0.08} _{-0.08}	5.72 ^{+0.63} _{-0.64}	4.79 ^{+0.22} _{-0.21}

Table 1. Evolution of bolometric luminosity (L_{bol}), blackbody radius (R_{bb}), and blackbody temperature (T_{bb}) obtained from blackbody fits to the spectral energy distribution of AT2019wxt at different epochs.

3.1.3. Bolometric Light Curve Evolution

The bolometric luminosity of AT2019wxt peaks at $\approx 1.96 \times 10^{42}$ erg s⁻¹ during the first observation. This is followed by a subsequent decline after which a second, lower luminosity peak is observed ($\approx 1.36 \times 10^{42}$ erg s⁻¹) at ≈ 3.1 days. After this, we observe a shallow decline in the bolometric luminosity. It should be noted that the L_{bol} value estimated from the first observation (via blackbody fits) has large uncertainty due to the lack of multi-band observations.

The blackbody temperature, T_{bb} , reaches a maximum value of ≈ 9770 K ≈ 1.5 days after the first observation, and rapidly decreases afterwards. At ≈ 3 days after the first observation, T_{bb} approaches a second peak with a maximum of ≈ 8320 K.

On the other hand, the blackbody radius of AT2019wxt increases over time and reaches a maximum ($\approx 22.76 \times 10^3 R_{\odot}$) at ≈ 12.7 days. The inverse trend in T_{bb} and R_{bb} evolution can be explained by an expanding envelope. Moreover, the high, initial temperature can be attributed to opaque, ionized material. As the matter expands and cools the opacity of this material should decrease with time due to recombination. Here, it is interesting to note that the reddening observed in the $g - i$ peaks at ≈ 12.7 days, which coincides with a maxima in blackbody radius R_{bb} and a minima in blackbody temperature.

We also compare the evolution of the bolometric luminosity, blackbody temperature, and blackbody radius of AT2019wxt to that of - i) kilonova AT2017gfo, ii) the USSNe candidates SN2019dgc and iPTF14gqr and iii) the Ca-rich gap transient iPTF16hgs in Figure 7. As evident from this Figure, the light curve of AT2019wxt evolves relatively slower than that of AT2017gfo (Abbott et al. (2017); Andreoni et al. (2017); Arcavi et al. (2017b); Coulter et al. (2017); Cowperthwaite et al. (2017); Drout et al. (2017); Evans et al. (2017); Nicholl et al. (2017); Kasliwal et al. (2017); Lipunov et al. (2017); Pian et al. (2017); Smartt et al. (2017); Tanvir et al. (2017); Troja et al. (2017); Utsumi et al. (2017); and Valenti et al. (2017)). Following the second peak in the blackbody temperature, T_{bb} , of AT2019wxt, the temperature steadily decreases faster than other USSNe candidates but in a manner analogous to iPTF16hgs a Ca-rich ‘‘gap’’ transient. Moreover, while the photospheric expansion for AT2019wxt is similar to other USSNe the contraction of the radius evolves on timescales intermediate to the kilonova and Ca-rich gap transients.

3.2. Spectroscopic Analysis

We present early-time spectra for AT2019wxt spanning a net waveband of 3000-10000 Å. These spectra were obtained from 2.45-2.75 days post initial peak and during the flux rise towards the second peak. In all of the spectra a blue continuum is observed which we fit with a `generic_continuum_fitting` routine available under the `astropy` spectroscopy package `Specutils`⁶. In this analysis, the continuum was modelled by smoothing with a median filter to remove the spikes. The source spectra was then normalised by dividing with the fitted continuum. To find significant lines in the spectra we used the `find_line_derivative` routine in `Specutils` which finds zero crossings in the spectrum derivative and depending on these, looks for lines above a certain threshold. In our line finding analysis, we set the threshold at $1-\sigma$ uncertainty in flux spectrum. A summary of significant lines and their presence in different spectra is presented in Table 2 and Fig. 8.

We observe multiple He I lines ($\lambda 5876$, $\lambda 6678$, $\lambda 7065$) and one He II $\lambda 4686$ line. Of the He I lines, we notice weakening of the He I $\lambda 6678$ as the source flux continues to rise, the

⁵ <https://github.com/dfm/emcee>

⁶ <https://specutils.readthedocs.io/en/stable/index.html>

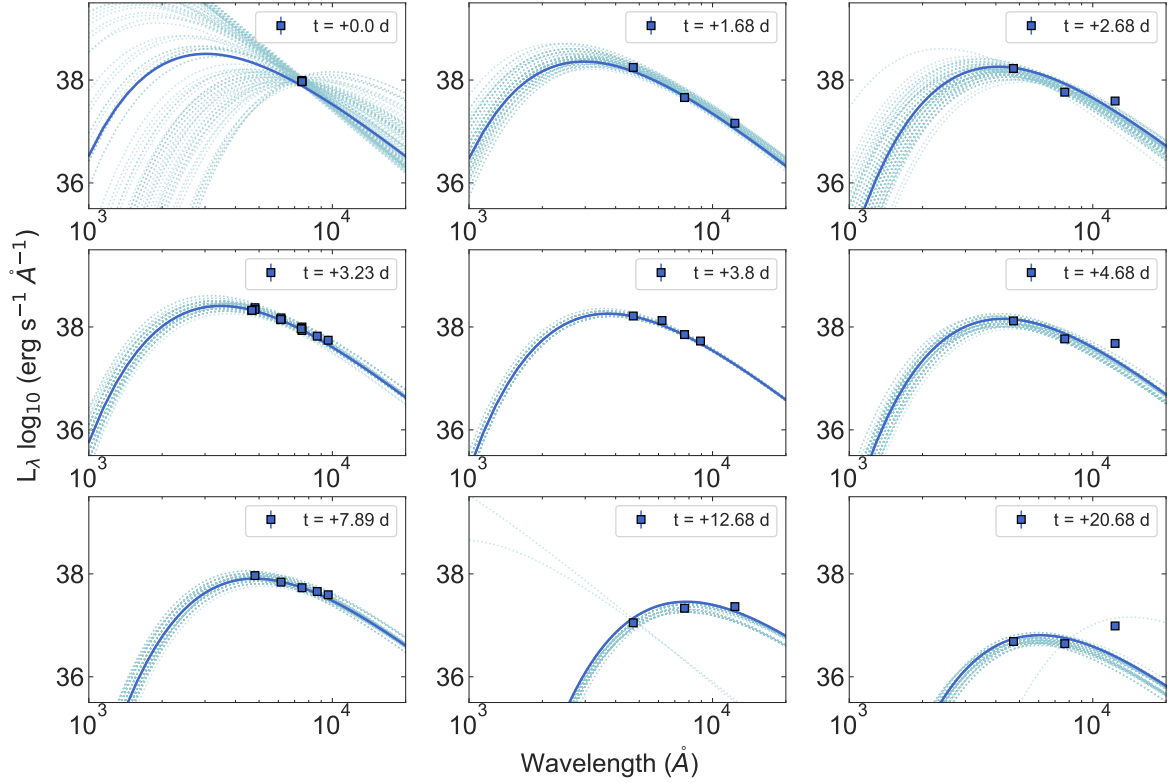


Figure 5. Spectral energy distribution (SED) evolution over eight epochs (days) for AT2019wxt. For each subplot, the square data points indicate the optical photometry at given wavelengths, the solid dark blue line represents the best fit blackbody model from the MCMC inference, and the dotted light blue lines represent the 100 random draws from the MCMC posterior.

Transition	HCT	ePESSTO+	VLT	LBT
He II $\lambda 4686$	✓	✓	✓	✓
He I $\lambda 5876$	✓	✓	✓	✓
He I $\lambda 6678$	✓	✓		
He I $\lambda 7065$	✓	✓	✓	✓
H α *	✓	✓	✓	✓
[C III] $\lambda 4650$	✓	✓	✓	✓
[C III] $\lambda 5696$	✓	✓		
[C IV] $\lambda 5801$	✓	✓	✓	✓
[O I] $\lambda 6300$	✓	✓		
[S II] $\lambda 6716$ *	✓	✓	✓	✓
[S II] $\lambda 6731$ *	✓	✓	✓	✓

Table 2. Summary of spectral lines observed in the early-time spectra of AT2019wxt for various instruments. The transition lines marked with an asterisk indicate host galaxy lines.

He II $\lambda 4686$ shows a similar attenuation. This line evolution behaviour is even more noticeable in C III ($\lambda 5696$) and O I $\lambda 6300$ lines which vanish over a course of 0.02 days between NTT and VLT-U1 observations. Another CIII line at $\lambda 4650$ is observed along with a weak C IV $\lambda 5801$. Finally, the SII

doublet lines - $\lambda 6716$ and $\lambda 6731$ - from the host galaxy. A prominent H α emission line from the galaxy is also observed.

3.3. Modeling the Double-Peaked light curve

Nakar & Piro (2014) show that in case of progenitors that are not enclosed by an extended envelope, only the blue bands exhibit a double-peaked structure in their light curve due to shock-cooling emission (SCE). In contrast, both the blue and red bands show a double-peaked light curve when an extended, low-mass envelope encloses the compact core. Given the redward nature of the i -band we infer that the double-peak structure observed in i -band light curves of AT2019wxt (see, Fig. 1) should indicate a presence of an extended envelope. Moreover, as we show earlier (Sec.1) light curves of core-collapse SNe which display double peaks in both blue and red bands have been explained in the past with combination of two kinds of emission processes - shock-cooling and radioactive decay of ^{56}Ni .

In this section, we follow a similar approach to derive light curve properties from multi-band optical and NIR observations of AT2019wxt. We explore a scenario such that the early-time emission is dominated by shock-cooling emission from an extended envelope followed by a late-time emission due to radioactive decay of ^{56}Ni . Hence, we model and subtract this early SCE component before fitting for radioactive decay of

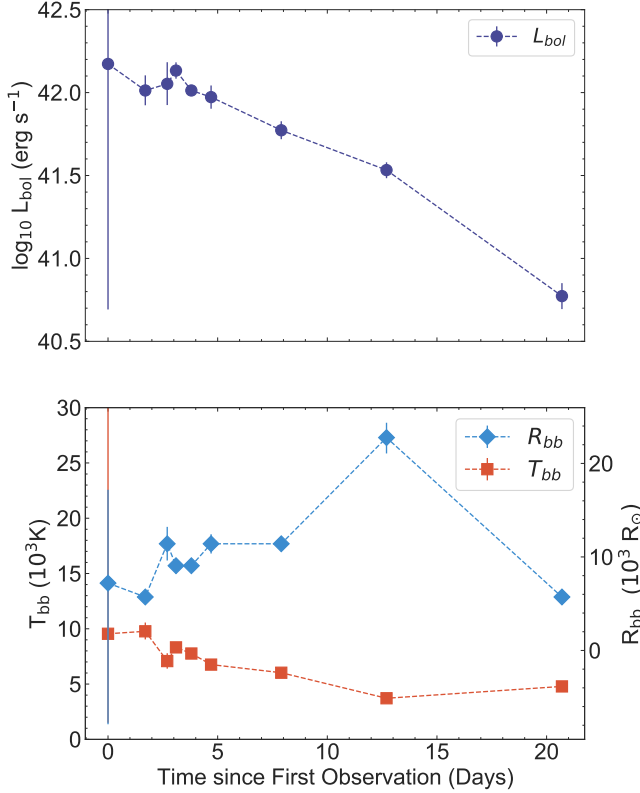


Figure 6. Time evolution of bolometric luminosity, blackbody temperature and blackbody radius obtained from the blackbody fits on the spectral energy distribution using the multi-color photometry for AT2019wxt using PAN-STARRS, Palomar, Lulin, DCT, and Wendelstein 2-m telescopes. All times are relative to the first optical observation as a reference epoch.

θ	Description	Prior
$\log R_{\text{ext}}$	\log_{10} of radius of extended envelope (cm)	$\mathcal{U}(1,18)$
$\log M_{\text{ext}}$	\log_{10} of mass of extended envelope (M_{\odot})	$\mathcal{U}(-4,-1)$
$E_{\text{ext},49}$	Energy in extended envelope divided by 10^{49} erg	$\mathcal{U}(0.1,20)$

Table 3. Parameters used for the early-time shock-cooling model and their priors.

^{56}Ni . This methodology has been successfully used in the past (Yao et al. 2020) to model USSNe with extended envelope.

We assume that for the early-time emission ($t < 2$ days; as seen in 1) of AT2019wxt, the emission is dominated by shock-cooling process. We used the Piro et al. (2021) shock-cooling model to constrain the SCE parameters such mass (M_{ext}), radius (R_{ext}), and energy ($E_{\text{ext},49}$) of the extended envelope. We fixed the time of the explosion for the model to $t_{\text{exp}} \approx -4$ days based on earliest upper limits available for AT2019wxt from our z -band observation. The SCE parameters were then assigned (wide) flat priors, as presented in Table 3. These priors were informed by low masses and large radii for extended envelopes inferred in previously known transients with early-time SCE. We perform the parameter inference using the emcee package MCMC implementation with a standard Gaussian log-

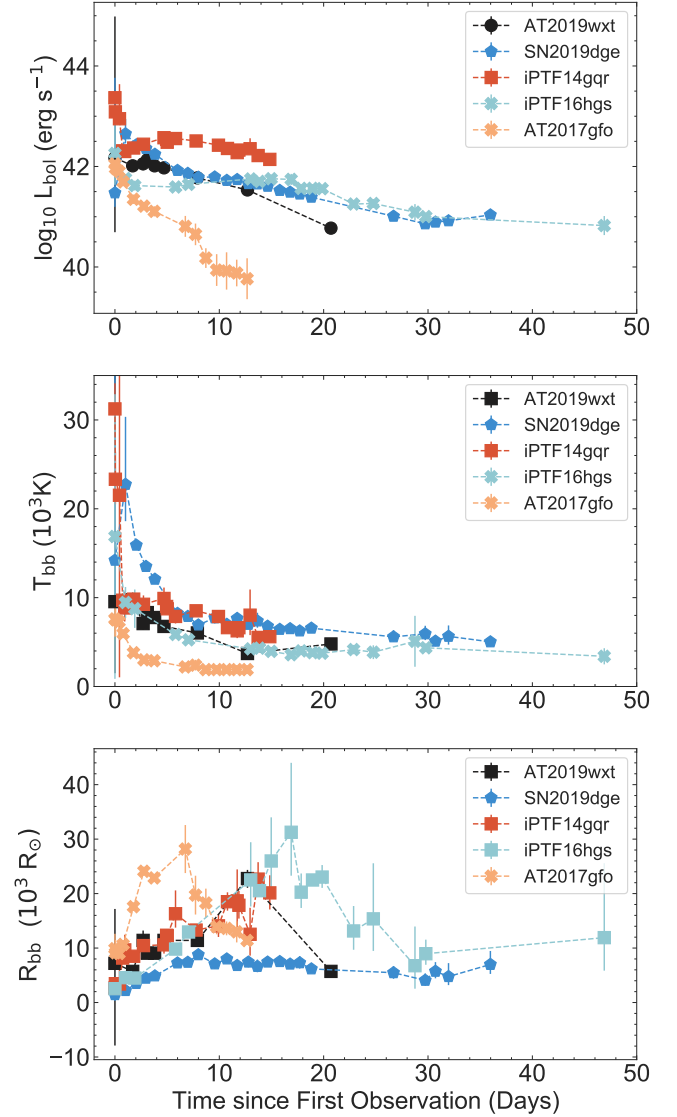


Figure 7. Time evolution of the bolometric luminosity, blackbody temperature, and blackbody radius of AT2019wxt compared with that of the USSN candidates SN2019dge and iPTF14gqr, Ca-rich gap transient iPTF16hgs, and the kilonova AT2017gfo. All times are relative to first optical observation used as a reference epoch for each transient.

likelihood function and with 100 walkers. The corner plot obtained from this analysis is displayed in Figure 13, which shows probability distributions for $\log_{10} M_{\text{ext}}$, $\log_{10} R_{\text{ext}}$, and $E_{\text{ext},49}$. We obtain the best-fitting model for parameter values of $M_{\text{ext}} = 3.55^{+0.12}_{-0.11} \times 10^{-2} M_{\odot}$, $R_{\text{ext}} = 5150.11^{+581.99}_{-513.27} R_{\odot}$, and $E_{\text{ext},49} = (10.00^{+6.82}_{-6.75}) \times 10^{49}$ erg.

We start the late-time emission ($t > 2$ days) fitting procedure by subtracting the best-fit SCE model from the initial light curve to infer the radioactivity-powered properties of AT2019wxt. We use the ^{56}Ni decay model by Valenti et al. (2008) to constrain the nickel mass (M_{Ni}), the characteristic photon diffusion timescale (τ_m), and the characteristic γ -ray timescale (t_0). The model parameters, are assigned wide, flat priors, as presented in Table 4. We again perform the parameter

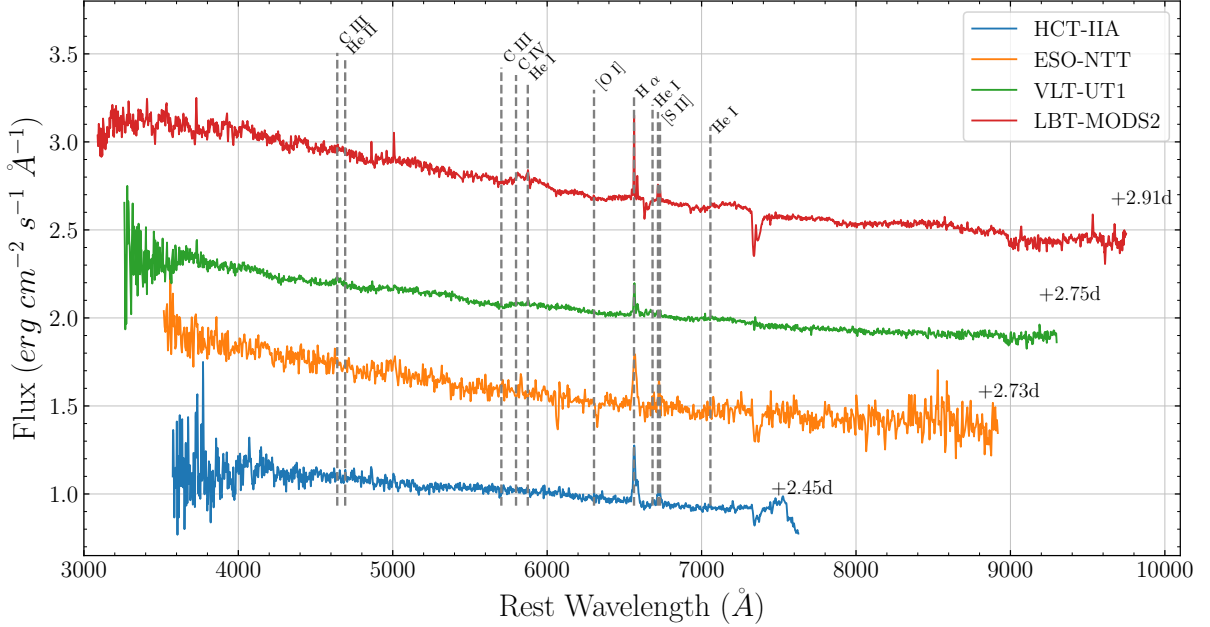


Figure 8. Early-time spectra of AT2019wxt arranged in order of their procurement from bottom to the top of the plot. These spectra were obtained with various telescopes such as HCT-IIA telescope at IAO-Hanle observatory, VLT and NTT. Each spectrum is normalised and presented with arbitrary offsets for ease of visualisation.

inference using the emcee package MCMC implementation with a standard Gaussian log-likelihood function involving 100 walkers. The corner plot obtained from this MCMC is displayed in Figure 14. We obtain the best-fit radioactivity model for parameter values of $M_{\text{Ni}} = 2.73^{+0.33}_{-0.18} \times 10^{-2} M_{\odot}$, $\tau_m = 4.35^{+1.16}_{-1.43}$ days, and $t_0 = 12.58^{+1.23}_{-1.34}$ days. The best-fit models for each of the shock-cooling emission and ^{56}Ni radioactive decay along with total luminosity evolution are presented in the figure 9.

θ	Description	Prior
τ_m	Characteristic photon diffusion time (day)	$\mathcal{U}(2,6)$
$\log M_{\text{Ni}}$	\log_{10} of nickel mass (M_{\odot})	$\mathcal{U}(-4,-1.25)$
t_0	Characteristic γ -ray escape time (day)	$\mathcal{U}(8,100)$

Table 4. Parameters used for the ^{56}Ni decay radioactivity model and their priors.

Based on our parameter estimations, we can calculate the ejecta mass using the an update to the ^{56}Ni decay model (see Equation 1 in Lyman et al. 2016):

$$M_{ej} = \left(\frac{\tau_m^2 \beta c v_{ph}}{2 \kappa_{opt}} \right) \quad (1)$$

where $\beta \approx 13.8$ is a constant, $\kappa_{opt} \approx 0.07 \text{ cm}^2 \text{ g}^{-1}$ is mean optical depth for a SESN, and v_{ph} is photospheric velocity ⁷.

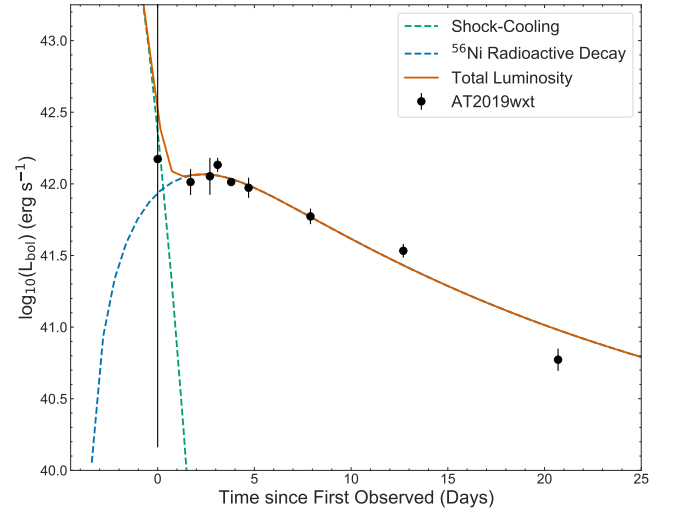


Figure 9. Bolometric light curve of AT2019wxt plotted with the best-fit shock-cooling model (dashed green line) and the best-fit ^{56}Ni decay radioactivity model (dashed blue line). The sum of the two models is shown in solid red line.

⁷ We substitute photospheric velocity (v_{ph}) in the equation in lieu of the usual “scale velocity” given v_{ph} is observationally equivalent to the scale velocity at the maximum bolometric luminosity.

In order to approximately calculate the ejecta mass for AT2019wxt, we assumed that photospheric velocity (v_{ph}) should be obtained close to the peak of the bolometric light curve. Therefore, to estimate this velocity we use the evolution of blackbody radius (R_{bb}) as an approximation for the change of photospheric radius. We then assume a linear expansion of the radius around the second peak (from $t = 1$ day to $t = 15$ days) to calculate the velocity of the ejecta. We find this ejecta velocity to be $\approx 9300 \text{ km s}^{-1}$.

Following from Equation 1 and estimated v_{ph} , we find the ejecta mass to be $M_{ej} \approx 0.20^{+0.12}_{-0.11} M_{\odot}$. This ejecta mass is of the same order of magnitude as the ejecta masses estimated for known USSN objects SN2019dge ($\approx 0.3 M_{\odot}$) and iPTF14gqr ($\approx 0.2 M_{\odot}$), which highlights the USSNe nature of AT2019wxt. This ejecta mass and velocity translate to AT2019wxt’s kinetic energy being $E_{kin,ej} \approx (1.01^{+0.61}_{-0.55}) \times 10^{50} \text{ erg}$. We would like to note that due to the assumptions in modelling the emission from AT2019wxt coupled with scarcity of early-time multi-band observations, there may exist degeneracies between the model parameters, such as between the radius and the energy of the extended envelope (Piro 2015).

3.4. X-ray Image Analysis

The primary analysis and calibration on X-ray data were performed with version 4.14 of *Chandra*’s CIAO software package (Fruscione et al. 2006). The calibration of X-ray data used the database CALDBv4.9.7. We reprocessed the primary and secondary data using the automatic *Chandra-repro* script, resulting in new level 2 event and response files.

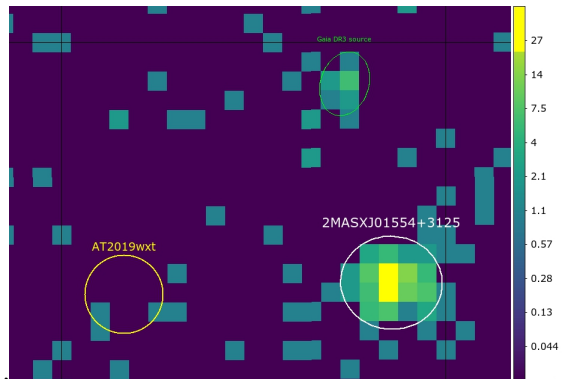


Figure 10. In this panel we present 0.3-10 keV *Chandra* image of AT2019wxt during the longest 100ks observation. We plot 1-arcsec radius circle centered optical position of AT2019wxt. The host galaxy active galactic nucleus (AGN) is indicated by an ellipse of major and minor axes 1.301” and 1.189”. We matched the coordinates of host galaxy from *Chandra* and find a match in both the NED and Gaia catalogs. The image colours are presented in log scale and we do not observe any significant emission at the location of AT2019wxt, while the host galaxy is confidently detected at the 5σ level. We also see a faint Gaia transient in the field.

After this, we obtained X-ray images for the 0.3-8keV energy range and used *wavdetect* to extract all the sources in the region. However, no sources were found in the region of

interest and spatially coincident with AT2019wxt. We used the *Chandra*’s *srcflx* routine to arrive at background count rates. This background rate allowed us to establish an upper limit on the source count rate. In this analysis we found the source to be undetectable at $6.51 \times 10^{-6} \text{ cts/s}$. We used absorbed power with an index of 2.1 and assumed a neutral Hydrogen density (N_H) of $1.8 \times 10^{20} \text{ cm}^{-2}$, to convert this count rate into a 0.3-8 keV flux upper limit of $\lesssim 9.93 \times 10^{-17} \text{ erg cm}^{-2} \text{ s}^{-1}$. Meanwhile, AGN of the host galaxy of AT2019wxt is detected with 5σ confidence threshold with count rate of $3.52 \times 10^{-3} \text{ cts s}^{-1}$. Using an absorbed power law with index of 1.7, this count rate corresponds to a flux of $5.87 \times 10^{-14} \text{ erg cm}^{-2} \text{ s}^{-1}$. The X-ray position for the galaxy coincides with the position reported in NED within the uncertainties.

3.5. Radio Data Analysis

Since all observations in the K band (22 GHz) were upper limits, we proceed to discuss results from only the X (10 GHz) and Ku (15 GHz) bands. Figure 11 shows the radio flux density measurements at the location of AT2019wxt (top panel) and the host galaxy, KUG 0152+311 (bottom panel) in the VLA X (10 GHz) and Ku (15 GHz) bands (see Table 10). The

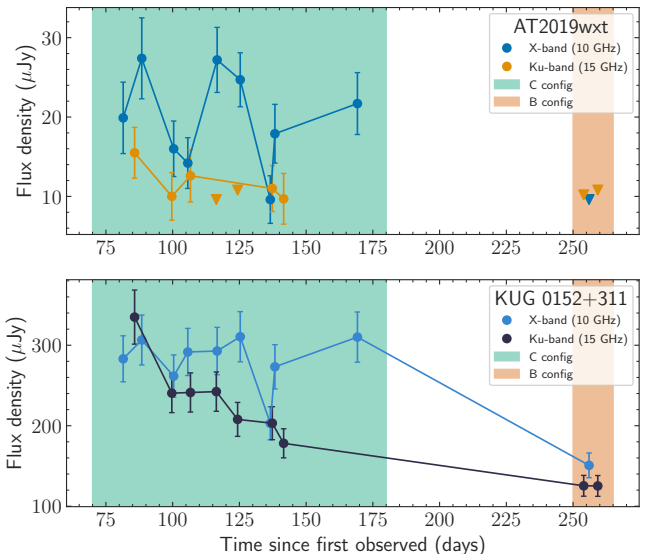


Figure 11. Plot of the radio flux density measurements at the location of AT2019wxt (top panel) in the X (10 GHz) and Ku (15 GHz), compared to the peak flux density measurements of the host galaxy (bottom panel) as a function of time, as reported in Table 10. The downward pointing triangles are upper limits (see Section 2.4 for more details).

host galaxy (KUG 0152+311) is resolved in images taken in X (10 GHz) and Ku (15 GHz) bands with the VLA in its C configuration and is marginally resolved in both these bands for the B configuration observations. Moreover, as evident from Figure 12, the host galaxy emission is likely contaminating our measurements at the location of AT2019wxt in observations taken with the VLA in its more compact C config-

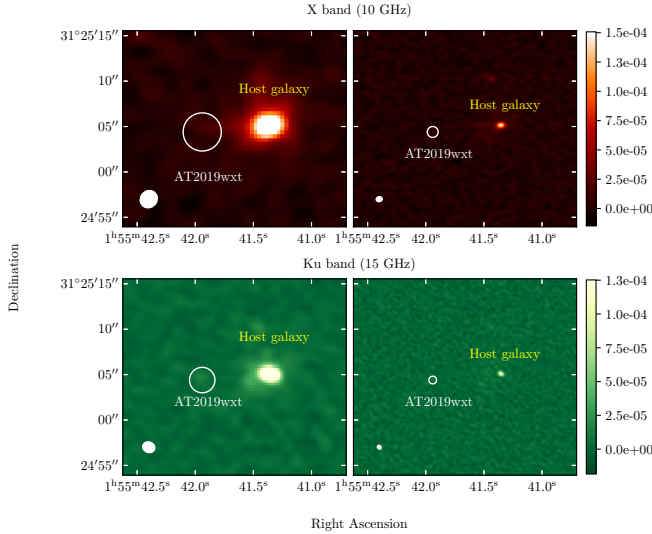


Figure 12. The host galaxy as seen in VLA configurations C (left) and B (right), in the X band (10 GHz, top) and Ku band (15 GHz, bottom). The white circles mark the position of AT2019wxt with a radius equal to the FWHM of the nominal VLA synthesized beam of each observation. The synthesised beam ellipse is shown on the left bottom of each panel and the colorbars provide the flux density in units of Jy. See text for discussion.

uration. A strong host galaxy contribution to the flux measured at the AT2019wxt location is also suggested by the fact that observations taken with the VLA in the more extended B configuration (see colored regions in Figure 11) show a drastic decrease in the measured flux density of the host galaxy, and return a non detection at the location of AT2019wxt (see also Table 10). This is compatible with the hypothesis that the more tenuous, extended emission from the host contaminates our C configuration measurements at the location of AT2019wxt, but goes undetected in the VLA B configuration (see also the right panels in Figure 12).

To test whether the flux we measure at the AT2019wxt location is dominated by host galaxy emission, we computed the Pearson correlation coefficient to check for a potential correlation between such flux and host galaxy flux density measurements (see e.g. D’Ammando et al. 2019; Hillier et al. 2019). We find that the flux measured at the AT2019wxt location is strongly correlated with that measured for the host galaxy (99.32% in the X band and 98.71% in the Ku band). This correlation can be visualised by comparing the time variation of the flux measurements at the AT2019wxt location, and that of the host galaxy (Figure 11). Next, to quantify the variability in the flux measurements obtained at the AT2019wxt location and for the AT2019wxt host galaxy, we use our X and Ku band data and adopt the statistical metrics described in Swinbank et al. (2015). We briefly introduce them here. We use N , F_ν and σ_ν to represent the number of observations, flux density measurements and the corresponding errors at frequency ν (see Table 10) respectively. The flux density coefficient of variation

can be calculated as:

$$V_\nu = \frac{1}{\overline{F_\nu}} \sqrt{\frac{N}{N-1} (\overline{F_\nu^2} - \overline{F_\nu}^2)}. \quad (2)$$

Assuming weights of $w_\nu = 1/\sigma_\nu^2$, the weighted average flux density is calculated as:

$$\xi_{F_\nu} = \frac{\sum_{i=1}^N w_\nu F_{\nu,i}}{\sum_{i=1}^N w_\nu}. \quad (3)$$

Further, we calculate the reduced- χ^2 using the above defined weighted mean flux density

$$\eta_\nu = \frac{1}{N-1} \sum_{i=1}^N \frac{(F_{\nu,i} - \xi_{F_\nu})^2}{\sigma_{\nu,i}^2}. \quad (4)$$

Using this metric we can calculate the probability for the source to be a variable as:

$$P_{\text{var}} = 1 - \int_{\eta'_\nu = \eta_\nu}^{\infty} p(\eta'_\nu, N-1) d\eta'_\nu. \quad (5)$$

where $p(x, n)$ is the χ^2 probability density function for x over n degrees of freedom.

Finally, we also compare the variability metrics computed for the flux measurements (excluding upper limits; see Table 10) at the location of AT2019wxt and the host galaxy, KUG 0152+311, with those that can be obtained from the radio light curves of the well-sampled radio-loud well-sampled Type IIb supernova SN1993J (Weiler et al. 2007) at the same timescales as our data. This comparison was made owing to the initial type IIb classification of the event (as discussed in Section 2.2.2).

Freq. band	AT2019wxt		Host		SN1993J	
	V_ν	$P_{\text{var}} (\%)$	V_ν	$P_{\text{var}} (\%)$	V_ν	$P_{\text{var}} (\%)$
X (10 GHz)	0.3	5.6	0.1	2.2	0.2	48.4
Ku (15 GHz)	0.2	3.3	0.2	32.6	0.2	4.2×10^{-3}

Table 5. Radio variability metrics for AT2019wxt compared with SN1993J in X (10 GHz) and Ku (15 GHz) bands excluding upper limits. See Section 3.5 for discussion.

As evident from Table 5, AT2019wxt and its host galaxy display comparable variability statistics in X-band. The last is much smaller than the variability of SN 1993J over the same timescales and in the same band. We also note that the same variability analysis for the X band (10 GHz) observations of GW170817 yields a variability statistic of $P_{\text{var}} = 55.7\%$ over timescales comparable to the ones of our radio observations of AT2019wxt. Thus, we exclude a GW170817-like radio counterpart for AT2019wxt.

The variability statistics in Ku band (15 GHz) is more complex. A SN 1993J-like transient would have varied very little in this band over the observed timescales. Hence, the lack

of substantial variability in this band would not necessarily indicate a host galaxy origin for the emission measured at the AT2019wxt location. Moreover, we note that in Ku band the flux from the core of the host varies substantially, and more than the flux measured at the position of AT2019wxt.

Overall our results suggest that the radio detections at the location of AT2019wxt are likely to be related to host galaxy contamination. There is little evidence for the type of variability that would be expected for SN 1993J-like or GW170817-like events.

4. DISCUSSION AND CONCLUSIONS

In this paper, we present optical, near-infrared, radio and X-ray observations and analysis for the peculiar and rapidly-evolving transient AT2019wxt. The source AT2019wxt was found on 2019 December 16 UTC 07:19:12 during the search for electromagnetic counterpart to the GW trigger S191213g. At the time it was prime optical counterpart of interest given its rapidly evolving light curve akin to kilonova expected from a binary neutron star merger. The source was intensely followed with *grizyJ* bands photometric and spectroscopic observations for approximately 20.7 days post initial discovery. The optical light curve shows a prominent double-peaked structure in the *i*-band and a less prominent structure in the *g*-band. The second peak has an absolute magnitude $g \sim i \sim -16.6$ mag. The bolometric light curve derived from the multi-band photometry displayed at least one peak, though with relatively large uncertainties. These uncertainties are a result of lack of multi-band observations of AT2019wxt in the early-time observations ($t \lesssim 2$ days). We characterise the optical/NIR light curve of AT2019wxt using a combination of early-time shock-cooling component and a late-time ^{56}Ni decay component. We estimate that the SCE arises from an extended envelope of mass $\approx 0.035 M_{\odot}$ and radius $\approx 35.8 \times 10^{13}$ cm. We also estimate that the radioactivity-powered component is composed of nickel mass $\approx 0.027 M_{\odot}$ from which we estimate the ejecta mass $\approx 0.20 M_{\odot}$.

Our long-term radio and X-ray observations of AT2019wxt spanned a period starting from 3.7 days after initial GW trigger discovery and up to 320 days. Our X-ray observations show no evidence for excess emission at the location of AT2019wxt. Previously, USSNe have been targeted with *Swift*-XRT observations (De et al. 2018b; Yao et al. 2020), however no X-ray emission was observed for these USSNe with multi-epochal X-ray observations at a flux threshold of $\lesssim 10^{-14}$ erg cm $^{-2}$ s $^{-1}$. In this work with long-term *Chandra* high-resolution X-ray observations of the source, we obtain one of the most stringent non-detection limits at $\lesssim 10^{-17}$ erg cm $^{-2}$ s $^{-1}$.

On the other hand, while our radio observations show excess emission at the location of AT2019wxt, there is little evidence for SN 1993j-like or GW170817-like variability over the timescales of our follow-up. We also discussed the possibility of host galaxy contamination at the location of AT2019wxt in the radio frequencies (especially at the lowest radio frequencies).

4.1. Transient Progenitor and Nature of the System

The double-peaked light curve in the *i*-band indicated presence of an extended envelope around the progenitor of AT2019wxt. This envelope likely originated from extreme stripping of the outer layers of this progenitor star (Nakar & Piro 2014). We find that the radius of the extended envelope inferred from our parameter estimation is an order of magnitude larger than those of previously known USSNe candidates (See Table 6). We would like to note that the uncertainties for the radius of the extended envelope are underestimated due to the lack of early-time observations, for which the shock-cooling model was fitted. For rapidly evolving transients such as USSNe, it is extremely critical to obtain observations in more than one bands (specifically, the redder bands) to get a better constraint on luminosity and rise time of the first peak. These early-time constraints can help provide a better estimate for the mass and radius of envelopes surrounding progenitors of USSNe. In addition to early-time multi-band observations, spectra taken during the first peak can help break the degeneracy between the the radius of the envelope and energy of the USSN by providing measurements of the velocity and composition of the extended material (Piro 2015).

An estimation of the ejecta mass can provide insight into the process likely causing the stripping of the outer layers of the progenitor. One of the mechanisms that can strip the envelope to this extent is binary mass transfer. Predictions from different stellar evolution models link the ejecta mass to the nature of the progenitor system. Single star evolutionary models of massive stars predict relatively high ejecta masses ($M_{ej} > 3 M_{\odot}$) (Meynet & Maeder 2005; Eldridge & Vink 2006; Georgy et al. 2009), much larger than that found for AT2019wxt ($M_{ej} \approx 0.20 M_{\odot}$). On the contrary, binary stellar evolution models predict that most Type Ib/c SNe emerged from massive stars in close binary systems, with ejecta mass ranging from $1 - 5 M_{\odot}$ (Dessart et al. 2012; Eldridge et al. 2013). An even greater degree of stripping can occur in a binary system further reducing ejecta masses to the order of $0.1 M_{\odot}$ and ^{56}Ni mass of the order of $0.01 M_{\odot}$ – as observed in USSNe (Tauris et al. 2013). These USSNe explosions are hence posited to be progenitors of double neutron star systems. The ejecta mass estimated for AT2019wxt is of the same order of magnitude as that of previously known USSNe candidates. Based on our photometric and spectroscopic analysis, we identify AT2019wxt as a strong USSNe candidate. While this paper was under development, the ENGRAVE collaboration (Agudo et al., in preparation) independently analysed AT2019wxt and arrived at similar conclusion for source characterisation.

Spectroscopic observations can provide a clue with respect to the extent of stripping that the progenitor underwent. However, given only two USSNe which are currently known we do not yet have a spectral model for these sources with characteristic features. However, some of the spectral lines that we list in Table 2 have been previously observed in both SN2019dge and iPTF14gqr sources. In our spectroscopic analysis we see no

Transient Name	Redshift	Host Galaxy Type	Second Peak Magnitude	Decay Rate (g-band) (mag day ⁻¹)	Ejecta Mass (M_{ej} (M_{\odot}))	Nickel Mass (M_{Ni} ($10^{-2}M_{\odot}$))	Envelope Radius (R_{ext} (10^{13} cm))	Envelope Mass (M_{ext} ($10^{-2}M_{\odot}$))
AT2019wxt	0.036	Compact	-16.6	0.41	$0.20^{+0.12}_{-0.11}$	$2.73^{+0.33}_{-0.18}$	$35.8^{+4.06}_{-3.68}$	$3.55^{+0.12}_{-0.11}$
SN2019dge	0.021	Compact	-15.5	0.13	$0.38^{+0.02}_{-0.02}$	$1.57^{+0.04}_{-0.03}$	$1.19^{+0.06}_{-0.05}$	$9.71^{+0.28}_{-0.27}$
iPTF14gqr	0.063	Spiral	-17.5	0.21	$0.24^{+0.02}_{-0.02}$	$8.14^{+0.14}_{-0.15}$	$6.09^{+8.73}_{-3.18}$	$2.59^{+0.46}_{-0.34}$
iPTF16hgs	0.017	Spiral	-15.1	0.17	$1.68^{+0.28}_{-0.25}$	$2.51^{+0.20}_{-0.22}$	$2.45^{+14.08}_{-1.80}$	$9.27^{+3.40}_{-2.48}$

Table 6. Parameters of different fast-evolving transients - Redshift of the host galaxy, host galaxy type, peak luminosity and decay rate with respect to the second peak of g -band observations, ejecta mass M_{ej} , nickel mass M_{Ni} , radius and mass of extended envelope R_{ext} , M_{ext}

broad Hydrogen lines indicating a loss of Hydrogen envelope in the system (Filippenko 1997).

AT2019wxt was located in a compact host galaxy, KUG 0152+311, at an offset of 0.5" S, 7.7" E from the galactic center. The USSNe candidate SN2019dge was also located in a compact host galaxy SDSS J173646.73 +503252.3 at a projected offset of 0.5" from the center. Meanwhile, the USSNe candidate iPTF14gqr was located in the outskirts of tidally interacting spiral galaxy IV Zw 155 at a projected offset of 24" from the center. The location of AT2019wxt at a relatively closer distance to the host galaxy's center matches with the prediction of Tauris et al. (2015) that USSNe are found to occur close to their host galaxy's star-forming regions.

4.2. AT2019wxt and searching for USSNe

Systematic all-sky surveys such as Zwicky Transient Facility (ZTF; Bellm et al. 2019; Graham et al. 2019) and intermediate Palomar Transient Factory (iPTF; Law et al. 2009) have accelerated searches for rapidly evolving transients (e.g. Ho et al. 2020; Andreoni et al. 2021). We can visualise the progress in transients searches in the last decade based on two key parameters: i) characteristic timescale of the transients- defined as the time taken for the magnitude to change by 0.75 mag from the peak, and ii) peak luminosity. A classification plot based on these quantities called the phase-space diagram (see, Fig. 1 Nugent et al. 2015) helps visualise spread between different transients such as SN, USSNe, stripped-envelope SN, kilonovae etc. In this plot, we observe that the transient AT2019wxt lies in the relatively slower-evolving and greater-luminosity regime compared to the kilonova AT2017gfo. However, post the second-peak it evolves faster compared to the USSNe candidates (SN2019dge and iPTF14gqr) and the Ca-rich gap transient (iPTF16hgs). It also shows black body parameters intermediate to kilonovae and USSNe as seen in Fig. 7. We expect upcoming wide-field surveys to open up a new discovery space for faster, fainter transients at large redshifts. A larger sample of transients populating the phase space diagram will be able to outline classes and sub-classes of transients such as SESNe (see, Fig. 18 Moriya et al. 2017).

The presence of an early-time peak in AT2019wxt is dominated by SCE. This SCE links to the progenitor stripping and highlights the importance of observing such rapidly-evolving

transients in the early stages. One of the main reasons this early-time peak was captured for AT2019wxt is that the source was coincidentally situated within the LIGO BNS merger region. Hence, global multi-band optical observation campaigns were launched to search for a rapidly-evolving counterpart to the GW trigger S191213g (Kasliwal et al. 2020). Andreoni et al. (2019) highlight the potential of high-cadence observational campaign of the Vera C. Rubin Observatory's Legacy Survey of Space and Time (LSST) (Ivezic et al. 2019) in capturing early SCE emission peak in SNe, which can provide important constraints on the progenitor star. Currently, only two USSNe candidates beyond AT2019wxt are known among nearly 10000 SNe found thus far. LSST is expected to improve SNe statistics up to a million SNe/yr (LSST Science Collaboration et al. 2009). Scaling to the first order from current ratio of USSNe to the SNe population, we expect ~ 20 USSNe/yr with LSST at larger redshifts. Early time peak capture of these USSNe will be important in arriving at properties of the source class as highlighted by AT2019wxt.

5. ACKNOWLEDGEMENTS

J.M.D. and H.S. acknowledge support from the Amsterdam Academic Alliance (AAA) Program, and the European Research Council (ERC) European Union's Horizon 2020 research and innovation program (grant agreement No. 679633; Exo-Atmos). This work is part of the research program VIDI New Frontiers in Exoplanetary Climatology, with project number 614.001.601, which is (partly) financed by the Dutch Research Council (NWO). F.H. and A.J. would like to thank observational support from Chandra X-ray observatory staff. Their work was supported by Chandra observational grant award GO0-21067X. A.B. and A.C. acknowledge support from the National Science Foundation via grant #1907975. The National Radio Astronomy Observatory is a facility of the National Science Foundation operated under cooperative agreement by Associated Universities, Inc. H.S. would like to thank Yuhao Yao for the methodologies developed to characterise USSNe that we have used in this work and for the insightful discussions throughout the course of this work. Nayana A.J. would like to acknowledge DST-INSPIRE Faculty Fellowship (IFA20-PH-259) for supporting this research.

REFERENCES

- 2001, *Astronomical Society of the Pacific Conference Series*, Vol. 229, *Evolution of Binary and Multiple Star Systems; A Meeting in Celebration of Peter Eggleton's 60th Birthday*
- Abbott, B. P., Abbott, R., Abbott, T. D., et al. 2017, *Phys. Rev. Lett.*, 119, 161101, doi: [10.1103/PhysRevLett.119.161101](https://doi.org/10.1103/PhysRevLett.119.161101)
- Andreoni, I., Ackley, K., Cooke, J., et al. 2017, *Publications of the Astronomical Society of Australia*, 34, e069, doi: [10.1017/pasa.2017.65](https://doi.org/10.1017/pasa.2017.65)
- Andreoni, I., Anand, S., Bianco, F. B., et al. 2019, *PASP*, 131, 068004, doi: [10.1088/1538-3873/ab1531](https://doi.org/10.1088/1538-3873/ab1531)
- Andreoni, I., Coughlin, M. W., Kool, E. C., et al. 2021, *ApJ*, 918, 63, doi: [10.3847/1538-4357/ac0bc7](https://doi.org/10.3847/1538-4357/ac0bc7)
- Arcavi, I., Hosseinzadeh, G., Howell, D. A., et al. 2017a, *Nature*, 551, 64, doi: [10.1038/nature24291](https://doi.org/10.1038/nature24291)
- Arcavi, I., McCully, C., Hosseinzadeh, G., et al. 2017b, *The Astrophysical Journal*, 848, L33, doi: [10.3847/2041-8213/aa910f](https://doi.org/10.3847/2041-8213/aa910f)
- Becerra-Gonzalez, J., & a larger Collaboration. 2019, *GRB Coordinates Network*, 26521, 1
- Begelman, M. C., & Sarazin, C. L. 1986, *ApJL*, 302, L59, doi: [10.1086/184637](https://doi.org/10.1086/184637)
- Bellm, E. C., Kulkarni, S. R., Graham, M. J., et al. 2019, *Publications of the Astronomical Society of the Pacific*, 131, 018002, doi: [10.1088/1538-3873/aaecbe](https://doi.org/10.1088/1538-3873/aaecbe)
- Bida, T. A., Dunham, E. W., Massey, P., & Roe, H. G. 2014, in *Society of Photo-Optical Instrumentation Engineers (SPIE) Conference Series*, Vol. 9147, *Ground-based and Airborne Instrumentation for Astronomy V*, ed. S. K. Ramsay, I. S. McLean, & H. Takami, 91472N, doi: [10.1117/12.2056872](https://doi.org/10.1117/12.2056872)
- Blagorodnova, N., Neill, J. D., Walters, R., et al. 2018, *PASP*, 130, 035003, doi: [10.1088/1538-3873/aaa53f](https://doi.org/10.1088/1538-3873/aaa53f)
- Cenko, S. B., Fox, D. B., Moon, D.-S., et al. 2006, *PASP*, 118, 1396, doi: [10.1086/508366](https://doi.org/10.1086/508366)
- Coulter, D. A., Foley, R. J., Kilpatrick, C. D., et al. 2017, *Science*, 358, 1556, doi: [10.1126/science.aap9811](https://doi.org/10.1126/science.aap9811)
- Cowperthwaite, P. S., Berger, E., Villar, V. A., et al. 2017, *The Astrophysical Journal*, 848, L17, doi: [10.3847/2041-8213/aa8fc7](https://doi.org/10.3847/2041-8213/aa8fc7)
- D'Ammando, F., Raiteri, C. M., Villata, M., et al. 2019, *MNRAS*, 490, 5300, doi: [10.1093/mnras/stz2792](https://doi.org/10.1093/mnras/stz2792)
- De, K., Kasliwal, M. M., Cantwell, T., et al. 2018a, *ApJ*, 866, 72, doi: [10.3847/1538-4357/aadf8e](https://doi.org/10.3847/1538-4357/aadf8e)
- De, K., Kasliwal, M. M., Ofek, E. O., et al. 2018b, *Science*, 362, 201, doi: [10.1126/science.aas8693](https://doi.org/10.1126/science.aas8693)
- Dessart, L., Hillier, D. J., Li, C., & Woosley, S. 2012, *Monthly Notices of the Royal Astronomical Society*, 424, 2139, doi: [10.1111/j.1365-2966.2012.21374.x](https://doi.org/10.1111/j.1365-2966.2012.21374.x)
- Dichiara, S., & a larger Collaboration. 2019, *GRB Coordinates Network*, 26517, 1
- Drout, M. R., Soderberg, A. M., Mazzali, P. A., et al. 2013, *ApJ*, 774, 58, doi: [10.1088/0004-637X/774/1/58](https://doi.org/10.1088/0004-637X/774/1/58)
- Drout, M. R., Piro, A. L., Shappee, B. J., et al. 2017, *Science*, 358, 1570, doi: [10.1126/science.aaq0049](https://doi.org/10.1126/science.aaq0049)
- Dutta, A., Kumar, B., Kumar, H., et al. 2019, *GRB Coordinates Network*, 26490, 1
- Eldridge, J. J., Fraser, M., Smartt, S. J., Maund, J. R., & Crockett, R. M. 2013, *Monthly Notices of the Royal Astronomical Society*, 436, 774, doi: [10.1093/mnras/stt1612](https://doi.org/10.1093/mnras/stt1612)
- Eldridge, J. J., & Vink, J. S. 2006, *Astronomy and Astrophysics*, 452, 295, doi: [10.1051/0004-6361/20065001](https://doi.org/10.1051/0004-6361/20065001)
- Evans, P. A., Cenko, S. B., Kennea, J. A., et al. 2017, *Science*, 358, 1565, doi: [10.1126/science.aap9580](https://doi.org/10.1126/science.aap9580)
- Filippenko, A. V. 1997, *ARA&A*, 35, 309, doi: [10.1146/annurev.astro.35.1.309](https://doi.org/10.1146/annurev.astro.35.1.309)
- Fitzpatrick, E. L. 1999, *The Publications of the Astronomical Society of the Pacific*, 111, 63, doi: [10.1086/316293](https://doi.org/10.1086/316293)
- Foley, R. J., Chornock, R., Filippenko, A. V., et al. 2009, *AJ*, 138, 376, doi: [10.1088/0004-6256/138/2/376](https://doi.org/10.1088/0004-6256/138/2/376)
- Foreman-Mackey, D., Hogg, D. W., Lang, D., & Goodman, J. 2013, *The Publications of the Astronomical Society of the Pacific*, 125, 306, doi: [10.1086/670067](https://doi.org/10.1086/670067)
- Fremling, C. 2019, *GRB Coordinates Network*, 26500, 1
- Fremling, C., Sollerman, J., Taddia, F., et al. 2016, *A&A*, 593, A68, doi: [10.1051/0004-6361/201628275](https://doi.org/10.1051/0004-6361/201628275)
- Fruscione, A., McDowell, J. C., Allen, G. E., et al. 2006, in *Society of Photo-Optical Instrumentation Engineers (SPIE) Conference Series*, Vol. 6270, *Society of Photo-Optical Instrumentation Engineers (SPIE) Conference Series*, ed. D. R. Silva & R. E. Doxsey, 62701V, doi: [10.1117/12.671760](https://doi.org/10.1117/12.671760)
- Gaia Collaboration. 2020, *VizieR Online Data Catalog*, I/350
- Gal-Yam, A., Arcavi, I., Ofek, E. O., et al. 2014, *Nature*, 509, 471, doi: [10.1038/nature13304](https://doi.org/10.1038/nature13304)
- Georgy, C., Meynet, G., Walder, R., Folini, D., & Maeder, A. 2009, *Astronomy and Astrophysics*, 502, 611, doi: [10.1051/0004-6361/200811339](https://doi.org/10.1051/0004-6361/200811339)
- Goodman, J., & Weare, J. 2010, *Communications in Applied Mathematics and Computational Science*, 5, 65, doi: [10.2140/camcos.2010.5.65](https://doi.org/10.2140/camcos.2010.5.65)
- Graham, M. J., Kulkarni, S. R., Bellm, E. C., et al. 2019, *PASP*, 131, 078001, doi: [10.1088/1538-3873/ab006c](https://doi.org/10.1088/1538-3873/ab006c)
- Haggard, D., Nynka, M., Ruan, J. J., et al. 2017, *ApJL*, 848, L25, doi: [10.3847/2041-8213/aa8ede](https://doi.org/10.3847/2041-8213/aa8ede)
- Hajela, A., Margutti, R., Bright, J. S., et al. 2022, *ApJL*, 927, L17, doi: [10.3847/2041-8213/ac504a](https://doi.org/10.3847/2041-8213/ac504a)
- Hillier, T., Brown, M. L., Harrison, I., & Whittaker, L. 2019, *MNRAS*, 488, 5420, doi: [10.1093/mnras/stz2098](https://doi.org/10.1093/mnras/stz2098)
- Ho, A. Y. Q., Perley, D. A., Kulkarni, S. R., et al. 2020, *ApJ*, 895, 49, doi: [10.3847/1538-4357/ab8bcf](https://doi.org/10.3847/1538-4357/ab8bcf)
- Hopp, U., Kluge, M., Goessl, C., Ries, C., & Schmidt, M. 2020, *GRB Coordinates Network*, 27057, 1

- Huber, M. E., Smartt, S. J., McBrien, O., & Schultz, K. C. C. A. S. B. 2019, GRB Coordinates Network, 26577, 1
- Ivezić, Ž., Kahn, S. M., Tyson, J. A., et al. 2019, *ApJ*, 873, 111, doi: [10.3847/1538-4357/ab042c](https://doi.org/10.3847/1538-4357/ab042c)
- Izzo, L., Malesani, D. B., Heintz, K. E., et al. 2019, GRB Coordinates Network, 26491, 1
- Jacobson-Galán, W. V., Margutti, R., Kilpatrick, C. D., et al. 2020, *ApJ*, 898, 166, doi: [10.3847/1538-4357/ab9e66](https://doi.org/10.3847/1538-4357/ab9e66)
- Kasliwal, M. M., Kulkarni, S. R., Gal-Yam, A., et al. 2010, *ApJL*, 723, L98, doi: [10.1088/2041-8205/723/1/L98](https://doi.org/10.1088/2041-8205/723/1/L98)
- Kasliwal, M. M., Nakar, E., Singer, L. P., et al. 2017, *Science*, 358, 1559, doi: [10.1126/science.aap9455](https://doi.org/10.1126/science.aap9455)
- Kasliwal, M. M., Anand, S., Ahumada, T., et al. 2020, *The Astrophysical Journal*, 905, 145, doi: [10.3847/1538-4357/abc335](https://doi.org/10.3847/1538-4357/abc335)
- Kong, A. 2019, GRB Coordinates Network, 26503, 1
- Kumar, B., Pandey, S. B., Sahu, D. K., et al. 2013, *MNRAS*, 431, 308, doi: [10.1093/mnras/stt162](https://doi.org/10.1093/mnras/stt162)
- Lang-Bardl, F., Bender, R., Goessl, C., et al. 2016, in *Society of Photo-Optical Instrumentation Engineers (SPIE) Conference Series*, Vol. 9908, Ground-based and Airborne Instrumentation for Astronomy VI, ed. C. J. Evans, L. Simard, & H. Takami, 990844, doi: [10.1117/12.2232039](https://doi.org/10.1117/12.2232039)
- Law, N. M., Kulkarni, S. R., Dekany, R. G., et al. 2009, *PASP*, 121, 1395, doi: [10.1086/648598](https://doi.org/10.1086/648598)
- LIGO Scientific Collaboration, & Virgo Collaboration. 2019a, GRB Coordinates Network, 26402, 1
- . 2019b, GRB Coordinates Network, 26417, 1
- Lipunov, V. M., Gorbvskoy, E., Kornilov, V. G., et al. 2017, *The Astrophysical Journal*, 850, L1, doi: [10.3847/2041-8213/aa92c0](https://doi.org/10.3847/2041-8213/aa92c0)
- LSST Science Collaboration, Abell, P. A., Allison, J., et al. 2009, arXiv e-prints, arXiv:0912.0201. <https://arxiv.org/abs/0912.0201>
- Lyman, J. D., Bersier, D., James, P. A., et al. 2016, *Monthly Notices of the Royal Astronomical Society*, 457, 328, doi: [10.1093/mnras/stv2983](https://doi.org/10.1093/mnras/stv2983)
- McBrien, O., Smartt, S. J., Smith, K. W., et al. 2019a, GRB Coordinates Network, 26485, 1
- McBrien, O. R., Smartt, S. J., Chen, T.-W., et al. 2019b, *The Astrophysical Journal*, 885, L23, doi: [10.3847/2041-8213/ab4dae](https://doi.org/10.3847/2041-8213/ab4dae)
- McLaughlin, S., Smartt, S. J., Smith, K. W., et al. 2019, *Transient Name Server AstroNote*, 154, 1
- McMullin, J. P., Waters, B., Schiebel, D., Young, W., & Golap, K. 2007, in *Astronomical Society of the Pacific Conference Series*, Vol. 376, *Astronomical Data Analysis Software and Systems XVI*, ed. R. A. Shaw, F. Hill, & D. J. Bell, 127
- Meynet, G., & Maeder, A. 2005, *Astronomy and Astrophysics*, 429, 581, doi: [10.1051/0004-6361:20047106](https://doi.org/10.1051/0004-6361:20047106)
- Moriya, T. J., Mazzali, P. A., Tominaga, N., et al. 2017, *Monthly Notices of the Royal Astronomical Society*, 466, 2085, doi: [10.1093/mnras/stw3225](https://doi.org/10.1093/mnras/stw3225)
- Müller Bravo, T., Chen, T. W., Fraser, M., et al. 2019, GRB Coordinates Network, 26494, 1
- Nakar, E., & Piro, A. L. 2014, *The Astrophysical Journal*, 788, 193, doi: [10.1088/0004-637X/788/2/193](https://doi.org/10.1088/0004-637X/788/2/193)
- Nicholl, M., Berger, E., Kasen, D., et al. 2017, *ApJL*, 848, L18, doi: [10.3847/2041-8213/aa9029](https://doi.org/10.3847/2041-8213/aa9029)
- Nugent, P., Cao, Y., & Kasliwal, M. 2015, in *Visualization and Data Analysis 2015*, ed. D. L. Kao, M. C. Hao, M. A. Livingston, & T. Wischgoll, Vol. 9397, *International Society for Optics and Photonics (SPIE)*, 1 – 7. <https://doi.org/10.1117/12.2085383>
- Pian, E., D’Avanzo, P., Benetti, S., et al. 2017, *Nature*, 551, 67, doi: [10.1038/nature24298](https://doi.org/10.1038/nature24298)
- Piro, A. L. 2015, *The Astrophysical Journal*, 808, L51, doi: [10.1088/2041-8205/808/2/L51](https://doi.org/10.1088/2041-8205/808/2/L51)
- Piro, A. L., Haynie, A., & Yao, Y. 2021, *The Astrophysical Journal*, 909, 209, doi: [10.3847/1538-4357/abe2b1](https://doi.org/10.3847/1538-4357/abe2b1)
- Podsiadlowski, P., Joss, P. C., & Hsu, J. J. L. 1992, *ApJ*, 391, 246, doi: [10.1086/171341](https://doi.org/10.1086/171341)
- Smartt, S. J., Chen, T. W., Jerkstrand, A., et al. 2017, *Nature*, 551, 75, doi: [10.1038/nature24303](https://doi.org/10.1038/nature24303)
- Smith, N., Li, W., Filippenko, A. V., & Chornock, R. 2011, *Monthly Notices of the Royal Astronomical Society*, 412, 1522, doi: [10.1111/j.1365-2966.2011.17229.x](https://doi.org/10.1111/j.1365-2966.2011.17229.x)
- Srivastav, S., & Smartt, S. J. 2019, GRB Coordinates Network, 26493, 1
- Stritzinger, M. D., Hsiao, E., Valenti, S., et al. 2014, *A&A*, 561, A146, doi: [10.1051/0004-6361/201322889](https://doi.org/10.1051/0004-6361/201322889)
- Swinbank, J. D., Staley, T. D., Molenaar, G. J., et al. 2015, *Astronomy and Computing*, 11, 25, doi: [10.1016/j.ascom.2015.03.002](https://doi.org/10.1016/j.ascom.2015.03.002)
- Tanvir, N. R., Levan, A. J., González-Fernández, C., et al. 2017, *The Astrophysical Journal*, 848, L27, doi: [10.3847/2041-8213/aa90b6](https://doi.org/10.3847/2041-8213/aa90b6)
- Tauris, T. M., Langer, N., Moriya, T. J., et al. 2013, *The Astrophysical Journal*, 778, L23, doi: [10.1088/2041-8205/778/2/L23](https://doi.org/10.1088/2041-8205/778/2/L23)
- Tauris, T. M., Langer, N., & Podsiadlowski, P. 2015, *Monthly Notices of the Royal Astronomical Society*, 451, 2123, doi: [10.1093/mnras/stv990](https://doi.org/10.1093/mnras/stv990)
- Tauris, T. M., Kramer, M., Freire, P. C. C., et al. 2017, *The Astrophysical Journal*, 846, 170, doi: [10.3847/1538-4357/aa7e89](https://doi.org/10.3847/1538-4357/aa7e89)
- The LIGO Scientific Collaboration, the Virgo Collaboration, the KAGRA Collaboration, et al. 2021, arXiv e-prints, arXiv:2111.03606. <https://arxiv.org/abs/2111.03606>
- Troja, E., Piro, L., van Eerten, H., et al. 2017, *Nature*, 551, 71, doi: [10.1038/nature24290](https://doi.org/10.1038/nature24290)
- Utsumi, Y., Tanaka, M., Tominaga, N., et al. 2017, *Publications of the Astronomical Society of Japan*, 69, 101, doi: [10.1093/pasj/psx118](https://doi.org/10.1093/pasj/psx118)
- Valeev, A. F., Castro-Rodriguez, N., & a larger Collaboration. 2019, GRB Coordinates Network, 26591, 1
- Valenti, S., Benetti, S., Cappellaro, E., et al. 2008, *Monthly Notices of the Royal Astronomical Society*, 383, 1485, doi: [10.1111/j.1365-2966.2007.12647.x](https://doi.org/10.1111/j.1365-2966.2007.12647.x)
- Valenti, S., Pastorello, A., Cappellaro, E., et al. 2009, *Nature*, 459, 674, doi: [10.1038/nature08023](https://doi.org/10.1038/nature08023)

- Valenti, S., Sand, D. J., Yang, S., et al. 2017, *The Astrophysical Journal*, 848, L24, doi: [10.3847/2041-8213/aa8edf](https://doi.org/10.3847/2041-8213/aa8edf)
- Vallely, P. 2019, GRB Coordinates Network, 26508, 1
- Vogl, C., Floers, A., Taubenberger, S., Hillebrandt, W., & Suyu, S. 2019, GRB Coordinates Network, 26504, 1
- Weiler, K. W., Williams, C. L., Panagia, N., et al. 2007, *ApJ*, 671, 1959, doi: [10.1086/523258](https://doi.org/10.1086/523258)
- Woosley, S. E., & Weaver, T. A. 1995, *ApJS*, 101, 181, doi: [10.1086/192237](https://doi.org/10.1086/192237)
- Yao, Y., De, K., Kasliwal, M. M., et al. 2020, *The Astrophysical Journal*, 900, 46, doi: [10.3847/1538-4357/abaa3d](https://doi.org/10.3847/1538-4357/abaa3d)
- Yoon, S.-C. 2017, *MNRAS*, 470, 3970, doi: [10.1093/mnras/stx1496](https://doi.org/10.1093/mnras/stx1496)
- Yoon, S. C., Woosley, S. E., & Langer, N. 2010, *The Astrophysical Journal*, 725, 940, doi: [10.1088/0004-637X/725/1/940](https://doi.org/10.1088/0004-637X/725/1/940)

APPENDIX

A. Observation Tables

Obs. Time (MJD)	Filter	Magnitude (mag)	Mag error (mag)
Pan-STARRS (McBrien et al. 2019a)			
58829.348	z	>21.0	–
58830.379	z	>20.3	–
58832.305	i	>19.4	–
58833.305	i	19.29	0.05
58833.320	i	19.23	0.07
58833.335	i	19.28	0.07
Palomar P60-inch (Fremling 2019)			
58836.687	g	19.43	0.10
58836.703	g	19.42	0.11
58836.684	r	19.28	0.11
58836.700	r	19.27	0.18
58836.690	i	19.28	0.13
58836.706	i	19.30	0.12
Lulin 1-m (Kong 2019)			
58836.446	g	19.32	0.04
58836.446	r	19.27	0.03
58836.446	i	19.38	0.06
DCT (Dichiara & a larger Collaboration 2019)			
58837.126	g	19.67	0.02
58837.114	r	19.30	0.02
58837.120	i	19.52	0.01
58837.126	z	19.51	0.03
Pan-STARRS (Huber et al. 2019)			
58836.434	g	19.23	0.09
58841.211	g	20.25	0.07
58836.436	r	19.19	0.07
58841.213	r	20.03	0.05
58836.438	i	19.21	0.07
58841.214	i	19.88	0.04
58836.439	z	19.34	0.11
58841.216	z	19.75	0.05
58836.441	y	19.31	0.22
58841.218	y	19.68	0.12
Wendelstein 2-m (Hopp et al. 2020)			
58835.000	g	19.59	0.08
58836.000	g	19.64	0.11
58838.000	g	19.91	0.06
58846.000	g	22.58	0.05
58854.000	g	23.49	0.08
58835.000	i	20.00	0.09
58836.000	i	19.74	0.09
58838.000	i	19.73	0.06
58846.000	i	20.82	0.06
58854.000	i	22.54	0.07
58835.000	J	20.22	0.08
58836.000	J	19.14	0.11
58838.000	J	18.92	0.10
58846.000	J	19.71	0.11
58854.000	J	20.65	0.12

Table 7. Summary of optical observations of AT2019wxt. The observation of AT2019wxt at MJD 58833.305 sets the reference epoch for this work.

Obs Start (MJD)	Telescope	Instrument	Wavelength (\AA)	Exposure time (s)	Resolution
58835.753	HCT-IIA	HFOSC2	3800-7500	3600	1200
58836.035	NTT-EPESSTO	EFOSC/1.57	3985-9315	1200.0061	18 \AA
58836.059	ESO-VLT-U1	CCDF-FORS2	3400-9600	1499.9388	10 \AA
58836.216	LBT	MODS2	3200-9750	3600	4 \AA

Table 8. Summary of optical spectroscopic observations of AT2019wxt.

Obs Id	Obs Start Time (MJD)	Effective Exposure (ks)
22458	58920.64792	49.41
23193	58922.27917	46.45
22459	59017.46736	42.51
23283	59018.33472	49.24
22460	59077.09375	33.45
22461	59152.85	19.82
24848	59153.8	14.89

Table 9. Summary of *Chandra* X-ray imaging observations of AT2019wxt, over a period of 233 days. All observations were obtained with ACIS-S3 chip in TE mode and VFaint telemetry format.

Obs. Time	Time Elapsed	VLA config.	VLA band	Obs. Freq.	Source Flux (μJy)	Galaxy Flux (μJy)
(MJD)	(days)			(GHz)	$F_\nu \pm \sigma_\nu$	peak $F_\nu \pm \sigma_\nu$
58837.0	3.7	D	K	22.0	< 25.1	452 \pm 91
58914.8	81.5	C	X	10.0	19.9 \pm 4.5	283 \pm 29
58919.1	85.7	C	Ku	15.4	15.5 \pm 3.2	335 \pm 34
58921.7	88.4	C	X	9.3	27.4 \pm 5.1	306 \pm 31
58933.0	99.7	C	Ku	15.4	10.0 \pm 3.0	240 \pm 24
58933.7	100.4	C	X	9.8	16.0 \pm 3.5	262 \pm 26
58939.0	105.7	C	X	10.0	14.2 \pm 3.2	292 \pm 29
58940.0	106.7	C	Ku	15.4	12.6 \pm 3.3	241 \pm 24
58943.7	110.4	C	K	22.0	< 21.6	152 \pm 31
58949.7	116.4	C	Ku	15.4	< 9.6	242 \pm 24
58950.0	116.7	C	X	9.7	27.2 \pm 4.1	293 \pm 29
58956.7	123.3	C	K	22.0	< 11.7	233 \pm 47
58957.6	124.3	C	Ku	15.3	< 10.8	208 \pm 21
58958.6	125.3	C	X	10.0	24.7 \pm 3.4	311 \pm 31
58969.9	136.6	C	X	10.0	9.6 \pm 3.0	203 \pm 20
58970.6	137.3	C	Ku	14.8	11.0 \pm 2.9	203 \pm 20
58971.6	138.3	C	X	9.3	17.9 \pm 3.7	273 \pm 28
58974.9	141.6	C	Ku	15.7	9.7 \pm 3.2	178 \pm 18
59002.5	169.2	C	X	9.4	21.7 \pm 3.9	310 \pm 31
59087.3	254.0	B	Ku	15.0	< 10.2	125 \pm 13
59089.3	256.0	B	X	10.0	< 9.6	151 \pm 15
59092.6	259.3	B	Ku	15.0	< 10.8	125 \pm 13

Table 10. VLA observations of AT2019wxt along with the integrated flux measurements of the host galaxy KUG 0152+311. All epochs are with respect to the first optical detection (MJD 58833.305). See Section 2.4 for more details.

B. Parameter Estimation

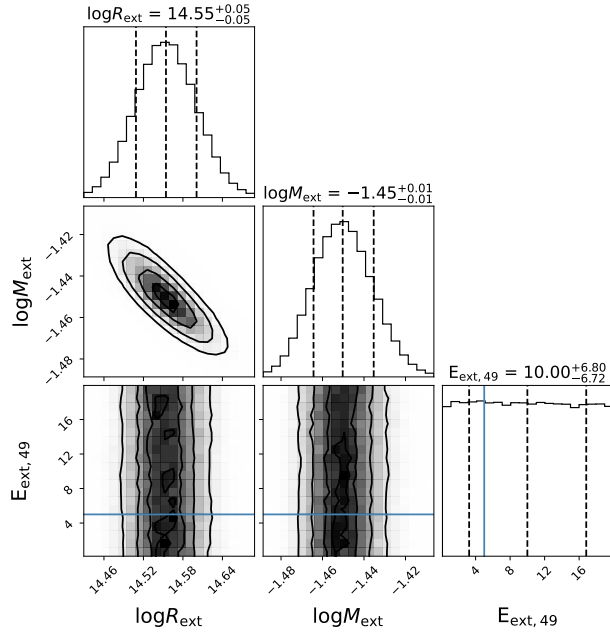


Figure 13. Corner plot obtained from the shock-cooling model displaying the constraints on the posteriors of \log_{10} of mass of the envelope ($\log M_{\text{env}}$), \log_{10} of radius of envelope ($\log R_{\text{env}}$), and energy of the envelope ($E_{\text{ext},49}$). Along the diagonal, the vertical dashed lines on the histogram indicate the estimate of the best-fit (median) value and the 68% confidence intervals. The contours represent the 16th, 50th and 84th percentile for the respective phase space.

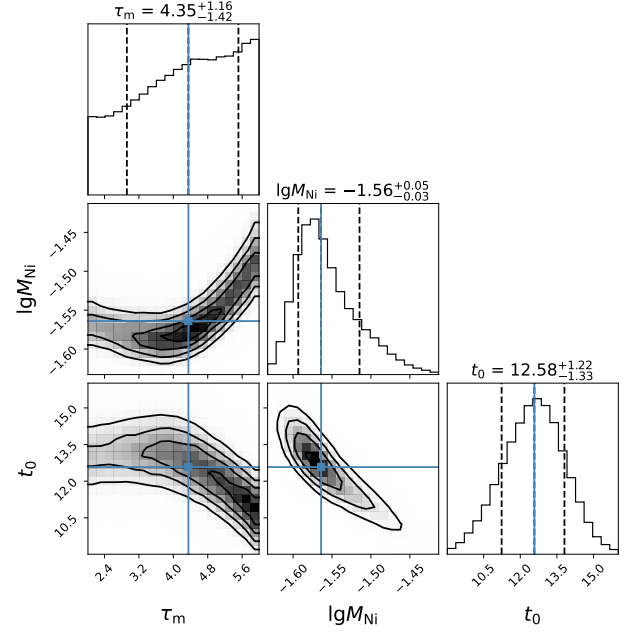


Figure 14. Corner plot obtained from the radioactivity model displaying the constraints on the posteriors of t_0 , $\log_{10} M_{\text{Ni}}$, and τ_m derived from the radioactivity model. Along the diagonal, the vertical dashed lines on the histogram indicate the estimate of the best-fit (median) value and the 68% confidence intervals. The contours represent the 16th, 50th and 84th percentile for the respective phase space.